The Astrophysical Journal, 948:112 (15pp), 2023 May 10 https://doi.org/10.3847/1538-4357/acc1e6
© 2023. The Author(s). Published by the American Astronomical Society.
OPEN ACCESS

# CLEAR: High-ionization [Ne V] λ3426 Emission-line Galaxies at $1.4 < z < 2.3$

Nikko J. Cleri[1,2,3], Guang Yang[1,2,4,5], Casey Papovich[1,2], Jonathan R. Trump[3], Bren E. Backhaus[3], Vicente Estrada-Carpenter[1,2,6], Steven L. Finkelstein[7], Mauro Giavalisco[8], Taylor A. Hutchison[1,2,9,17], Zhiyuan Ji[8], Intae Jung[10,11,12], Jasleen Matharu[1,2,13], Ivelina Momcheva[14,15], Grace M. Olivier[1,2], Raymond Simons[15], and Benjamin Weiner[16]

[1] Department of Physics and Astronomy, Texas A&M University, College Station, TX 77843-4242 USA; cleri@tamu.edu
[2] George P. and Cynthia Woods Mitchell Institute for Fundamental Physics and Astronomy, Texas A&M University, College Station, TX 77843-4242 USA
[3] Department of Physics, University of Connecticut, Storrs, CT 06269, USA
[4] Kapteyn Astronomical Institute, University of Groningen, P.O. Box 800, 9700 AV Groningen, The Netherlands
[5] SRON Netherlands Institute for Space Research, Postbus 800, 9700 AV Groningen, The Netherlands
[6] Department of Astronomy & Physics, Saint Mary's University, 923 Robie Street, Halifax, NS B3H 3C3, Canada
[7] Department of Astronomy, The University of Texas, Austin, TX 78712 USA
[8] Department of Astronomy, University of Massachusetts Amherst, 710 N. Pleasant Street, Amherst, MA 01003, USA
[9] Astrophysics Science Division, NASA Goddard Space Flight Center, 8800 Greenbelt Road, Greenbelt, MD 20771, USA
[10] Department of Physics, The Catholic University of America, Washington, DC 20064, USA
[11] Astrophysics Science Division, Goddard Space Flight Center, Greenbelt, MD 20771, USA
[12] Center for Research and Exploration in Space Science and Technology, NASA/GSFC, Greenbelt, MD 20771, USA
[13] Cosmic Dawn Center, Niels Bohr Institute, University of Copenhagen, Rådmandsgade 62, DK-2200 Copenhagen, Denmark
[14] Max-Planck-Institut für Astronomie, Königstuhl 17, D-69117 Heidelberg, Germany
[15] Space Telescope Science Institute, 3700 San Martin Drive, Baltimore, MD, 21218 USA
[16] MMT/Steward Observatory, 933 N. Cherry Street, University of Arizona, Tucson, AZ 85721, USA
*Received 2022 September 13; revised 2023 February 27; accepted 2023 March 3; published 2023 May 12*

## Abstract

We analyze a sample of 25 [Ne V] (λ3426) emission-line galaxies at $1.4 < z < 2.3$ using Hubble Space Telescope/Wide Field Camera 3 G102 and G141 grism observations from the CANDELS Lyα Emission at Reionization (CLEAR) survey. [Ne V] emission probes extremely energetic photoionization (creation potential of 97.11 eV) and is often attributed to energetic radiation from active galactic nuclei (AGNs), shocks from supernovae, or an otherwise very hard ionizing spectrum from the stellar continuum. In this work, we use [Ne V] in conjunction with other rest-frame UV/optical emission lines ([O II] λλ3726, 3729, [Ne III] λ3869, Hβ, [O III] λλ4959, 5007, Hα +[N II] λλ6548, 6583, [S II] λλ6716, 6731), deep (2–7 Ms) X-ray observations (from Chandra), and mid-infrared imaging (from Spitzer) to study the origin of this emission and to place constraints on the nature of the ionizing engine. The majority of the [Ne V]-detected galaxies have properties consistent with ionization from AGNs. However, for our [Ne V]-selected sample, the X-ray luminosities are consistent with local ($z \lesssim 0.1$) X-ray-selected Seyferts, but the [Ne V] luminosities are more consistent with those from $z \sim 1$ X-ray-selected QSOs. The excess [Ne V] emission requires either reduced hard X-rays or a ∼0.1 keV excess. We discuss possible origins of the apparent [Ne V] excess, which could be related to the "soft (X-ray) excess" observed in some QSOs and Seyferts and/or be a consequence of a complex/anisotropic geometry for the narrow-line region, combined with absorption from a warm, relativistic wind ejected from the accretion disk. We also consider implications for future studies of extreme high-ionization systems in the epoch of reionization ($z \gtrsim 6$) with the James Webb Space Telescope.

*Unified Astronomy Thesaurus concepts:* Active galaxies (17); AGN host galaxies (2017); High-redshift galaxies (734); Quasars (1319); Seyfert galaxies (1447); Ultraviolet spectroscopy (2284); Optical astronomy (1776); Reionization (1383); Photoionization (2060)

## 1. Introduction

Studies from modern observatories like the Hubble Space Telescope (HST) have shown that cosmic star formation density peaked roughly 7–11 billion years ago ($z \sim 1$–3), an epoch when the properties of galaxies were fundamentally different than at present (Madau & Dickinson 2014). Understanding the physical conditions in galaxies at these redshifts and beyond is paramount, especially as we move into the era of the James Webb Space Telescope (JWST), where we expect to see increasing numbers of "chemically young" (i.e., low-metallicity) galaxies, which are likely key contributors to the reionization of the universe. These rapidly star-forming galaxies exhibit prominent high-ionization nebular emission lines in their rest-frame ultraviolet (UV) and optical spectra, suggesting that these reionization-era galaxies are characterized by extreme radiation fields (e.g., Brinchmann 2022; Katz et al. 2023; Trump et al. 2023).

The underlying physics of these high-ionization systems of the epoch of reionization (EoR, $z > 6$) remain poorly understood, and much of the information about the EoR is extrapolated from local metal-poor dwarf galaxies (e.g., Berg et al. 2019, 2021; Olivier et al. 2022). One means to test the ionizing sources in galaxies across cosmic time is through ratios of strong optical and near-UV emission lines, which serve as useful diagnostics of conditions in the interstellar

[17] NASA Postdoctoral Fellow.

Original content from this work may be used under the terms of the Creative Commons Attribution 4.0 licence. Any further distribution of this work must maintain attribution to the author(s) and the title of the work, journal citation and DOI.

medium (ISM) (e.g., Kewley et al. 2019b). Much of the knowledge of the physics of higher-redshift star formation is derived from bright Balmer lines of hydrogen (H$\alpha$ and H$\beta$), along with lines of oxygen ([O II] $\lambda\lambda$3726, 3728 and [O III] $\lambda\lambda$4959, 5007), sulfur ([S II] $\lambda\lambda$6717, 6731) and nitrogen ([N II] $\lambda$6584). This suite of near-UV/optical emission lines used for spectral classifications of galaxies is optimized for observation by HST around the peak of cosmic star formation at $z\sim2$, where these lines are redshifted into the near-IR.

Previous work using this suite of emission features in the optical and near-UV have shown that, for galaxies around cosmic noon ($z\sim2$), oxygen abundances are lower, ionization parameters are higher, and ionization fields are harder at stellar masses similar to those of $z\sim0$ galaxies (e.g., Erb et al. 2006; Nakajima & Ouchi 2014; Steidel et al. 2014; Tang et al. 2021).

Other bright near-UV/optical emission lines remain largely unexplored. The high-ionization lines of neon have only been studied slightly, focusing on the [Ne III] $\lambda$3869 (40.96–63.45 eV) line (e.g., Levesque & Richardson 2014; Masters et al. 2014; Zeimann et al. 2015; Backhaus et al. 2022). These works have shown that [Ne III] traces [O III] emission and that the [Ne III]/[O II] ratio can be used as a spectral classifier of active galactic nuclei (AGNs) and star formation in conjunction with [O III]/H$\beta$.

In this work, we study an even higher energy near-UV emission feature: quadruply ionized neon ([Ne V] $\lambda\lambda$3346, 3426). The energy required to produce [Ne V] photons (97.11–126.21 eV) is extremely high compared to other bright UV/optical emission lines; the minimum bound is nearly triple that of [O III] (35.12 eV) and nearly double that of ionized helium, He II (54.42 eV), which denotes the boundary of "high ionization" and "very high ionization" in the four-zone ionization model of Berg et al. (2021).

The production of such a high-ionization emission line requires an extreme photoionizing source. Studies attribute [Ne V] production to photoionization from AGNs, stellar light from the extremely hot ionizing spectra (e.g., Wolf–Rayet stars), or energetic shocks from supernovae (Gilli et al. 2010; Izotov et al. 2012; Mignoli et al. 2013; Zeimann et al. 2015; Backhaus et al. 2022).

Studies of local star-forming galaxies have attempted to explain the [Ne V] production through energetic supernova shocks. Izotov et al. (2012) find five oxygen-poor blue compact dwarf (BCD) galaxies with [Ne V] emission that have [Ne V]/He II flux ratios reproducible by radiative shock models with shock velocities in the 300–500 km s$^{-1}$ range and shock ionizing contributions $\sim$10% that of stellar continuum ionization. However, this modeling cannot conclusively discount this $\sim$10% contribution, responsible for [Ne V] emission, from being produced by AGNs. These studies have primarily focused on low-mass galaxies (BCDs in the case of Izotov et al. 2012). However, there are other examples, including Leung et al. (2021), that studied extended [Ne V] emission in the local ultraluminous infrared galaxy Mrk 273 and showed that [Ne V] is consistent with production from shocks for this object. Therefore, shocked gas is also a viable mechanism for [Ne V] emission in and around galaxies.

Emission from [Ne V] has been used to study conditions in the narrow-line region (NLR) in AGNs. Gilli et al. (2010) and Mignoli et al. (2013) used [Ne V] luminosities in conjunction with hard-band (2–10 keV) X-ray luminosities to probe highly obscured/Compton-thick (CT) AGNs. These analyses with [Ne V] luminosities are inspired by similar analyses using X-ray and [O III] luminosities (Maiolino et al. 1998; Heckman et al. 2005; Yan et al. 2011; Lambrides et al. 2020), with the added benefit of the extreme energies required to produce [Ne V]. Gilli et al. (2010) and Mignoli et al. (2013) conclude that galaxies with very low ($<$15) X-ray/[Ne V] luminosity ratios are effectively all CT AGNs, though the relation of the absorption column densities ($N_{\rm H}$) from X-ray spectral fits to the X-ray/[Ne V] ratio is highly dependent on model assumptions (Li et al. 2019). Therefore, while low X-ray-to-[Ne V] ratios indicate CT AGNs in Seyferts and higher-redshift QSOs, such data have not been extended to more modest galaxies (including the galaxies that dominate the cosmic star formation rate (SFR) density (Madau & Dickinson 2014) and SMBH accretion (Hickox & Alexander 2018).

In this work, we study the properties of galaxies with [Ne V] at redshifts $1.4<z<2.3$. We combine the [Ne V] emission with information from several of the other bright rest-frame UV/optical emission-line features of [Ne III], [O III], [O II], H$\beta$, H$\alpha$, and [S II], to study the physical characteristics of highly ionizing radiation in galaxies around the peak of cosmic star formation at $z\sim2$. Because these lines trace a range of ionization state, they offer direct traces of multiple phases in the ISM (Berg et al. 2021). By studying multiple transitions within the same (and multiple) elements, we can more clearly understand the chemical characteristics of a galaxy.

Understanding this population of high-ionization galaxies has important implications for studies of the EoR with JWST (e.g., Rhoads et al. 2023; Trump et al. 2023; Katz et al. 2023). The Near-IR Camera (NIRCam) and Near-IR Spectrograph (NIRSpec) on JWST have the wavelength coverage to detect these extreme [Ne V]-emitting galaxies at $0.8\lesssim z\lesssim14$, and the Near-IR Imager and Slitless Spectrograph (NIRISS) will give slitless spectroscopy of [Ne V] at lower redshifts ($3<z<7$). These objects are sure to be critical targets in spectroscopic surveys with JWST in the near future.

The remainder of this work is as follows: Section 2 describes our parent sample from the CLEAR survey and our selection of [Ne V] sources. Section 3 compares UV/optical emission-line ratios as diagnostics of AGN activity. Section 4 explores the X-ray/[Ne V] ratio along with X-ray and [Ne V] luminosity functions. Section 5 discusses the implications of our results. Section 6 summarizes the results of this work and discusses future studies of high-ionization galaxies with JWST and the Nancy Grace Roman Space Telescope.

Throughout this work, we assume a flat $\Lambda$CDM cosmology with $H_0=70$ km s$^{-1}$ Mpc$^{-1}$ and $\Omega_M=0.30$ (Planck Collaboration et al. 2020).

## 2. Data

Our data come from the CANDELS Ly$\alpha$ Emission at Reionization (CLEAR)[18] survey (a Cycle 23 HST program; PI: Papovich; Simons et al. 2023), which consists of deep (12-orbit depth) HST/WFC3 G102 slitless grism spectroscopy covering 0.8–1.15 $\mu$m within 12 fields split between the GOODS-North (GN) and GOODS-South (GS) extragalactic survey fields (Estrada-Carpenter et al. 2019; Simons et al. 2021). The CLEAR pointings overlap with the larger 3D-HST survey area (Momcheva et al. 2016), which provides slitless

[18] https://clear.physics.tamu.edu

G141 grism spectra of two-orbit depth with spectral coverage of 1.1–1.65 $\mu$m.

These data will be described fully in the forthcoming survey paper on the data release (Simons et al. 2023) and have been discussed in other works using these data (e.g., Estrada-Carpenter et al. 2019, 2020; Simons et al. 2021; Backhaus et al. 2022, 2023; Cleri et al. 2022; Jung et al. 2022; Matharu et al. 2022; Papovich et al. 2022).

### 2.1. G102 and G141 Spectroscopy, Redshifts, and Line Fluxes

The `grizli` (grism redshift and line analysis) pipeline[19] serves as the primary method of data reduction for the CLEAR data set. In contrast to traditional methods of extracting one-dimensional (1D) spectra from slit observations, `grizli` directly fits the two-dimensional (2D) spectra with model spectra convolved to the galaxy image for multiple position angles of grism observations. This process yields complete and uniform characterization of the suite of spectral line features of all objects observed in each of the G102 and G141 grisms. The flux calibrations of the G102 and G141 spectra are, in general, accurate to within a few (∼3) percent (Lee et al. 2014; Pirzkal et al. 2016, 2017; Estrada-Carpenter et al. 2019). The most relevant of these spectral properties for our analysis are redshifts, line fluxes, and emission-line maps. The [Ne V] doublet at 3346 and 3426 Å is fit with a free ratio, i.e., `grizli` does not force a ratio of [Ne V] $\lambda3426/$[Ne V] $\lambda3346 = 2.73$ (the expected ratio under typical nebular conditions; see Figures 8 and 9 in Appendix A).

In this work, we use the CLEAR v4.1 catalogs (Simons et al. 2021). The data products of these catalogs include emission-line fluxes, spectroscopic redshifts, and other derived quantities and their respective uncertainties for 6048 objects from the `grizli` run on the combination of the G102 and G141 grism data and broadband photometry using the 3D-HST+ catalogs. Of these galaxies, 4707 galaxies have coverage with both G102 and G141, which constitutes the initial catalog that we used to identify galaxies for our study here. The emission-line fluxes from the `grizli` reduction presented in this work are not corrected for attenuation by dust in the ISM.

The uncertainties of the emission lines account for the uncertainties of the continuum model, as they are fit simultaneously. We note that the low spectral resolution may bias our sample to large equivalent widths, and the uncertainties in the continuum may lead to more uncertain equivalent widths than higher-resolution samples.

### 2.2. Photometry and Derived Quantities

We use stellar masses for objects in our sample from the 3D-HST catalog (Skelton et al. 2014), derived from the CANDELS photometry (Grogin et al. 2011; Koekemoer et al. 2011). The stellar masses are calculated by modeling the spectral energy distribution (SED) with FAST (Kriek et al. 2009), using a Bruzual & Charlot (2003) stellar population synthesis model library, a Chabrier (2003) initial mass function, and solar metallicity and assuming exponentially declining star formation histories. The stellar masses of our galaxies are generally robust to these assumptions because the peak of the stellar emission is well constrained by the high-quality CANDELS near-IR imaging. Stellar masses from the 3D-HST survey have a mass limit at $z \sim 2$ of $\log(M_*/M_\odot) \sim 8.5$ for $H < 25$ (Skelton et al. 2014).

To place these galaxies in context, we also compare their SFRs to other galaxies at similar redshifts. For this purpose, we use UV continuum SFRs from the Cosmic Assembly Near-infrared Deep Extragalactic Legacy Survey (CANDELS)/Survey for High-$z$ Absorption Red and Dead Sources (SHARDS) catalog of Barro et al. (2019), which supplements the CANDELS multiwavelength data with SHARDS photometry (Pérez-González et al. 2013) in GN and GS. Attenuation-corrected UV SFRs are calculated using the Kennicutt (1998) calibration with a dust attenuation correction. This is fully described in Barro et al. (2019).

### 2.3. Parent Data Set and Sample Selection

Our parent sample represents all CLEAR galaxies within the redshift range for detectable [Ne V] and [O III] in the G102 and G141 spectrum ($1.39 < z < 2.40$). Requiring the wavelength coverage of a strong line such as [O III] eliminates many potentially spurious objects from the prospective sample and secures reliable spectroscopic redshifts for each object. The wavelength limits of this selection are set by the coverage of the blue end of the G102 and the red end of the G141 grisms (8000 and 16500 Å, respectively). The CLEAR spectral extractions are limited to galaxies with $m_{\rm F105W} < 25$.

We select a sample of [Ne V]-emitting galaxies from the CLEAR parent catalog using the following steps:

1. Require a grism spectroscopic redshift, $1.39 < z < 2.30$, such that both [Ne V] lines and [O III] are all within the observed-frame spectral range of G102 and G141 sensitivity (0.8–1.65 $\mu$m).
2. Require signal-to-noise ratio (S/N) of 3 for the stronger line of the [Ne V] doublet (3426 Å) and [O III].
3. Visual inspection of direct images with 1D and 2D spectra.

This last step ensures that no objects with poor continuum modeling and/or bad contamination subtraction make it into the final selection (this is a known issue with slitless spectroscopy, and visual inspection is important, especially for studies of objects with faint(er) emission lines like ours here; e.g., Zeimann et al. 2014, 2015; Estrada-Carpenter et al. 2019, 2020; Backhaus et al. 2022, 2023). Each object was inspected by at least three authors. This selection rejects ∼40% of objects that pass the first two criteria.

After applying all these selection processes, we have a sample of 25 [Ne V]-emitting objects in CLEAR within the allowable redshift range of the G102 and G141 grisms ($1.39 < z < 2.30$). In our sample, all galaxies have [O III] S/N > 5 (significantly greater than the minimum requirement of S/N > 3). This lends greater credence to the spectroscopic redshifts and line identification. We also note that 9/25 objects have [Ne V] S/N > 5; the implications of the veracity of the [Ne V] detections are discussed in Section 5. Our sample comprises approximately 2.6% of all objects in the CLEAR catalog in this redshift range.

Our final sample has a redshift range of $1.40 < z < 2.29$, with a median grism redshift of 1.61. The redshift distribution of the 25 [Ne V]-detected galaxies in our sample is shown in Figure 1. It is fairly evenly distributed in redshift, with a possible spike at $z \sim 1.6$, which corresponds to the known

[19] https://github.com/gbrammer/grizli/

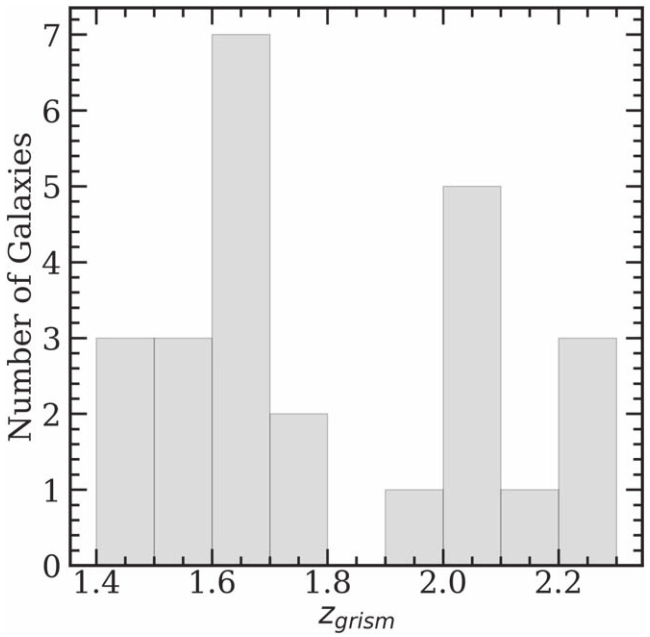


**Figure 1.** Grism redshift distribution of our sample of 25 [Ne V] galaxies. The G141 grism wavelength range limits the detection of [Ne V] and [O III] to $1.39 < z < 2.30$. Our sample has a redshift range of $1.40 < z < 2.29$, with a median grism redshift of 1.61. The spike in sources at $z \sim 1.6$ is consistent with an overdensity of sources in GS at this redshift.

overdensity of galaxies at this redshift in the GS field (Estrada-Carpenter et al. 2019). The properties and derived quantities (including line fluxes) for the galaxies in our sample are shown in Tables 1 and 2.

Figure 2 shows rest-frame 1D spectra of five [Ne V]-emitting objects in the CLEAR sample, ordered by increasing redshift. The points and error bars shown in the 1D spectra are the medians in each bin of wavelength over all exposures. The points are separated into G102 (blue) and G141 (red). We note the region around several lines of interest: [Ne V] $\lambda\lambda$3346, 3426, [O II] $\lambda\lambda$3726, 3729, [Ne III] $\lambda$3869, H$\gamma$, H$\beta$, and [O III] $\lambda\lambda$4959, 5007.

Figure 3 shows the relation between star formation derived from attenuation-corrected UV luminosity and stellar mass, from Barro et al. (2019). Our sample is again broadly consistent with CLEAR toward lower stellar mass. All but three of our [Ne V]-emitting galaxies lie within the 95% contours of the CLEAR parent population. Eight objects lie between the 85% and 95% contours, indicating that nearly half of the galaxies in our sample have elevated SFRs compared to the rest of CLEAR. One of these objects (GS 42758) has the highest attenuation-corrected UV SFR in the sample and has a $V$-band attenuation of 1.1 mag (Skelton et al. 2014), and it is also an X-ray AGN (see Section 2.4). The rest of the sample is consistent with low dust: we see a median $V$-band attenuation for the sample of 0.3 mag.

### 2.4. Comparison with X-Ray AGN Catalogs

The CLEAR fields include the deepest X-ray imaging from Chandra available anywhere on the sky (7 Ms in GS and 2 Ms in GN; see Luo et al. 2017 and Xue et al. 2016, respectively). We use the X-ray luminosity for galaxies to diagnose their AGN activity. We matched our sample with the X-ray catalogs for the Chandra Deep Field North and South (CDF-N and CDF-S; Xue et al. 2016; Luo et al. 2017). Classifications from these catalogs include "AGN," "galaxy," and "star," where the AGN classification must satisfy at least one of the following four criteria from Xue et al. (2011), that is, we combine these with a logical OR:

1. $L_{0.5-7\,\mathrm{keV}} \geqslant 3 \times 10^{42}\,\mathrm{erg\,s^{-1}}$ (consistent with luminous AGN);
2. effective photon index $\Gamma \leqslant 1.0$ (evidence for Obscured AGN);
3. X-ray-to-optical flux ratio of $\log(f_X/f_R) > -1$, where $f_X = f_{0.5-7\,\mathrm{keV}}$, $f_{0.5-2\,\mathrm{keV}}$, or $f_{2-7\,\mathrm{keV}}$ (evidence for AGN origin of X-ray emission);
4. excess X-ray emission over expectation from pure star formation $L_{0.5-7\,\mathrm{keV}} \geqslant 3 \times (8.9 \times 10^{17}\,L_R)$,

where $f_X$, $L_X$, $f_R$, and $L_R$ are the X-ray and $R$-band fluxes and luminosities, respectively. Objects labeled as "galaxies" in the X-ray catalogs are those that are confirmed to be galaxies (e.g., not stars/objects with a redshift of 0) but do not meet any of these criteria. This selection is subject to the caveat that luminous starbursts may be able to produce sufficient X-ray emission from X-ray binaries to be classified as AGNs (Lehmer et al. 2010).

Matching with our [Ne V] sample, we find eight objects with X-ray detections classified as AGNs. Throughout this work, we will denote these X-ray-detected AGNs in figures with a cross where appropriate. This selection alone suggests that [Ne V] is a useful tracer of AGN activity: 32% (8/25) of the [Ne V] sample are classified as X-ray AGNs, while only 6.5% of the rest of the CLEAR galaxies at this redshift range are classified as X-ray AGNs.

### 2.5. Comparison with IR AGN Catalogs

In addition to the X-ray matching to select potential AGNs, we also select objects that are identified as AGNs by mid-IR photometry. We use photometry from the Infrared Array Camera (IRAC) on Spitzer (Fazio et al. 2004; Lacy et al. 2004; Stern et al. 2005). Our IR color selection criteria are outlined in Donley et al. (2012) and Coil et al. (2015), designed to limit contamination by star-forming galaxies to $z < 3$ while maintaining reliability and completeness. For the following selection, our notation is such that

$$x = \log_{10}\left(\frac{f_{5.8\mu\mathrm{m}}}{f_{3.6\mu\mathrm{m}}}\right), \quad y = \log_{10}\left(\frac{f_{8.0\mu\mathrm{m}}}{f_{4.5\mu\mathrm{m}}}\right). \tag{1}$$

The selection of IR AGNs from Donley et al. (2012) requires all of the following criteria:

1. objects are detected in all four IRAC channels (peak wavelengths 3.6, 4.6, 5.8, and 8.0 $\mu$m);
2. $x \geqslant 0.08$ and $y \geqslant 0.15$;
3. $y \geqslant 1.21x - 0.27$;
4. $y \leqslant 1.21x + 0.27$;
5. $f_{8.0\mu\mathrm{m}} > f_{5.8\mu\mathrm{m}} > f_{4.5\mu\mathrm{m}} > f_{3.6\mu\mathrm{m}}$.

This selection identifies two objects in our [Ne V]-detected CLEAR sample as IR AGNs. Both objects identified through this photometric selection are also identified as X-ray AGNs in the selection given in Section 2.4. IR AGN selection generally samples more luminous AGNs than X-ray selection (Mendez et al. 2013). Consequently, it is unsurprising to find that the two IR AGNs in our sample are also X-ray detected.

This selection, similarly to the X-ray AGN selection, suggests that [Ne V] emission traces AGN activity: 10.5% of

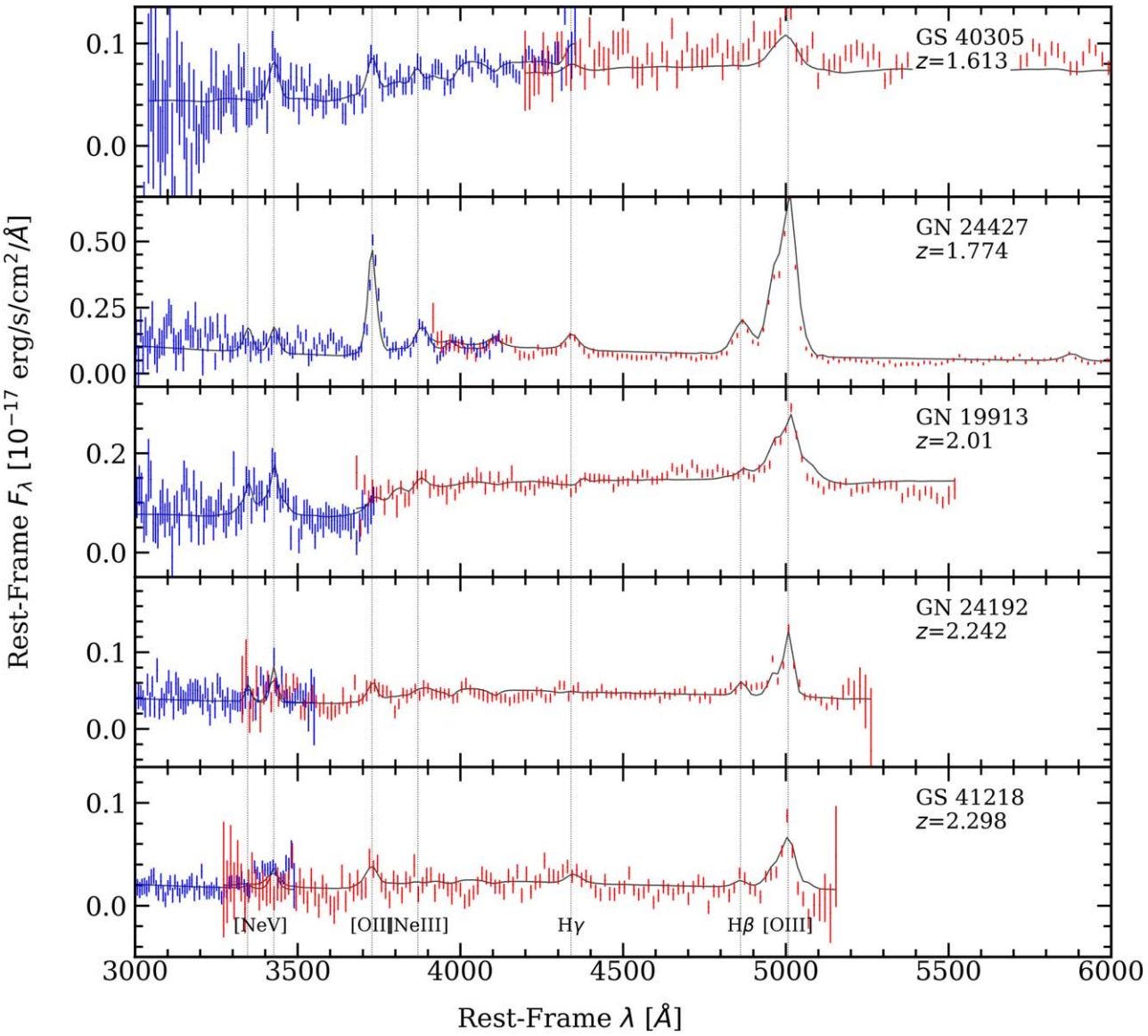


**Figure 2.** Rest-frame 1D spectra for five [Ne V]-emitting objects in the CLEAR sample, ordered by increasing redshift. The G102 (blue) and G141 (red) spectra show the median points with $1\sigma$ uncertainties from all exposures for this object. The dotted lines indicate emission features of interest: [Ne V] $\lambda\lambda$3346, 3426, [O II] $\lambda\lambda$3726, 3729, [Ne III] $\lambda$3869, H$\gamma$ $\lambda$4340, H$\beta$ $\lambda$4861, and [O III] $\lambda\lambda$4959, 5007.

the [Ne V] sample are classified as IR AGNs, while only 1.4% of the rest of the CLEAR galaxies at this redshift range are classified as IR AGNs.

## 3. Spectral Classification of Star Formation and AGN Activity

To characterize the source of ionizing radiation for each galaxy in our [Ne V] sample, we primarily use the [O III]/H$\beta$ ratio combined with other diagnostics. When [O III]/H$\beta$ ratios are compared to other galactic parameters (e.g., stellar mass and other line ratios), the relation can be used to diagnose the "activity" of the galaxy: "active" galaxies hosting AGN or "inactive" galaxies dominated by star formation.

### 3.1. The Mass–Excitation Diagram

We start by considering the "mass–excitation" (MEx) diagram, which combines the [O III]/H$\beta$ ratio with the stellar mass (Juneau et al. 2011, 2014). The MEx diagram is the most inclusive of these AGN diagnostics, i.e., it is suitable for galaxies even in the case in which we have only one line ratio, [O III]/H$\beta$. The dependence of the MEx diagnostic on stellar mass includes biases and assumptions of SED modeling (Barro et al. 2019). Juneau et al. (2014) derived empirical demarcations between AGNs and galaxies with star formation. First, they set a relation between [O III]/H$\beta$ and stellar mass that identifies galaxies with ionization from only AGNs, defined to have $y \equiv \log([\mathrm{O\,III}]/\mathrm{H}\beta)$[20] greater than the value given by the relationship

$$y = \begin{cases} \frac{0.375}{(x-10.5)} + 1.14, & x \leqslant 9.9 \\ 410.24 - 109.333x & \\ +9.71731x^2 - 0.288244x^3, & \text{otherwise} \end{cases}, \quad (2)$$

[20] For the HST G102 and G141 grism spectral resolution, the [O III] $\lambda\lambda$4959, 5007 lines are blended, so we use the blended flux for these analyses.

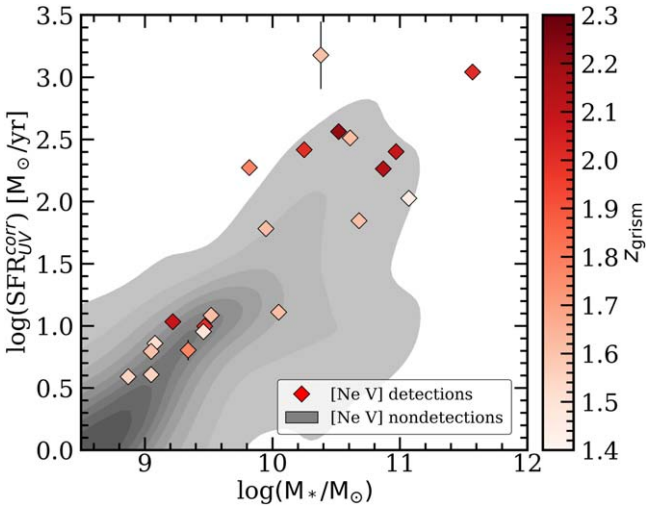


**Figure 3.** The relation between attenuation-corrected UV SFR and stellar mass for galaxies of redshift $1.39 < z < 2.30$. Our sample of [Ne V]-emitting galaxies is shown as diamonds color-coded by grism redshift, with the rest of the CLEAR galaxies with derived UV SFRs in this redshift range shown as gray contours. We show the $1\sigma$ uncertainties in the attenuation-corrected UV SFRs for the [Ne V] detections, most of which are smaller than the marker size. The lower-mass objects in our sample are broadly consistent with the rest of the CLEAR sample in SFR–mass space; however, our sample includes several objects with higher mass/SFR than expected compared to the parent population, with 11/25 objects outside of the second-to-last (85%) contour, 3 of which are outside of the last (95%) contour.

where $x \equiv \log(M_*)$. Second, they use a relation between line ratio and stellar mass, where galaxies below this line ratio contain ionization from only star formation, where $y$ for this relation is given by

$$y = 352.066\text{–}93.8249x + 8.32651x^2\text{–}0.246416x^3 \quad (3)$$

in the range $9.9 < \log(M_*) < 11.2$. To summarize, galaxies that lie above the top curve (Equation (2)) in the MEx diagram are classified as AGNs; galaxies that lie below the bottom curve (Equation (3)) are classified as star-forming. We further define galaxies that lie between these two curves as composite sources, with contributions from both AGNs and star formation.

However, we need to adjust the MEx diagram to account for redshift evolution. For example, Coil et al. (2015) studied a population of AGNs at $z \sim 2.3$ with rest-frame optical emission-line ratios. They concluded that they needed to apply a shift of $\Delta \log(M_*/M_\odot) = 0.75$ dex, which more accurately separates star-forming galaxies and AGNs at this redshift. This provides a more pure selection of confirmed X-ray AGNs via the MEx diagram than the local Juneau et al. (2014) line.

Here we use the MEx relation and adopt a shift intermediate between that of Juneau et al. (2014) and Coil et al. (2015), as the CLEAR [Ne V] sample lies at a median redshift $z \sim 1.61$, between that of the samples of these other studies. We construct a simple empirical model to encapsulate this shift in the MEx relation from redshift evolution. This expands on the 0.75 dex shift from Juneau et al. (2014) to Coil et al. (2015), which becomes

$$x = \log(M_*) + 0.2(1 + z), \quad (4)$$

where $x$ is defined above and $0.2(1 + z)$ represents the shift in the $x$-axis from the Juneau et al. (2014) line (Equations (2) and (3)). We arrive at this shift of $0.2(1 + z)$, as it classifies all X-ray-confirmed AGNs with stellar mass $\log(M_*/M_\odot) > 9$ as AGNs or $1\sigma$ consistent with the AGN/SF dividing line. This shift keeps the same purity of the Coil et al. (2015) AGN selection, but (as we discuss below) this is more consistent with the X-ray-detected [Ne V] sources in our sample, which would otherwise be labeled star-forming by the Coil et al. (2015) line.

Figure 4 (left panel) shows the MEx diagnostic for the galaxies in our CLEAR [Ne V] sample (where we include all of our galaxies that have S/N > 1 in H$\beta$ and [O III]). The diamonds show the 18 sources in our [Ne V] sample that satisfy this requirement. We denote galaxies in our CLEAR [Ne V] sample detected in X-rays with a thin cross, and we denote galaxies that satisfy the IR AGN definition with a hollow cross. We also show on the MEx diagram those galaxies detected with S/N > 1 in CLEAR without [Ne V] detections, in the same redshift range as the [Ne V] sample, as small gray points.

Roughly half of the sources in our [Ne V] sample lie in the AGN region of the MEx plot. If we compare to the MEx definition defined by Juneau et al. (2014), then 12/18 (=66%) of the sources in the CLEAR [Ne V] sample show evidence of AGN ionization. This includes all of the sources detected in X-rays or identified as IR AGNs. Using the MEx definition of Coil et al. (2015), this fraction drops to 8/18 (44%) and misses two of the X-ray sources but includes all the IR AGNs. When we compare the MEx selection using the redshift offset for our [Ne V] sample (assuming the median redshift of the sample $z = 1.61$ with Equation (4), as indicated by the solid lines in the MEx panel of Figure 4), we would select 11/18 (61%) of the [Ne V] sources, including all the X-ray sources and IR AGNs.

The results of this MEx analysis are broadly consistent with previous work done with [Ne V] galaxies. Mignoli et al. (2013) find that an AGN fraction of ~80% of [Ne V]-emitting galaxies at $z \sim 0.8$ is consistent with AGN classification via MEx, although the analyses are not directly comparable, as Mignoli et al. (2013) use the Juneau et al. (2011) $z \lesssim 0.1$ MEx division and do not perform the same redshift evolution of the MEx line as in this work. Given the relatively small sample in this work, as well as the biases of MEx and stellar mass derivations, we caution against use of this diagnostic when others are available (see Section 5 for more discussion).

### 3.2. The "OHNO" Diagram

We next explore other emission-line diagnostics designed to separate galaxies with ionization from AGNs and star formation. One such diagnostic is the [O III]/H$\beta$ and [Ne III]/[O II] (the "OHNO") diagram (Zeimann et al. 2015; Backhaus et al. 2022). This diagnostic compares ratios of emission lines at similar wavelengths ([O II] $\lambda\lambda$3726, 3729, [Ne III] $\lambda$3869, H$\beta$ $\lambda$4861, and [O III] $\lambda\lambda$4959, 5007) where the production of [O III] and the production of [Ne III] both require higher photon energies: the ionization energy of $O^0$ is 13.6 eV, that of $O^+$ is 35.1 eV, and that of $Ne^+$ is 41.0 eV. Galaxies with strong [O III]/H$\beta$ and/or [Ne III]/[O II] require harder radiation fields, typically found in the emission-line regions of AGNs. Backhaus et al. (2022) showed that division in the OHNO line ratios separates X-ray-selected AGNs from non-AGNs (based on classifications from the deep X-ray data in the CDF-N and CDF-S fields).

The middle panel of Figure 4 shows the OHNO diagram for the galaxies in our CLEAR sample. The redshift range that allows for all five of these lines in the HST G102 and G141 grism coverage is $1.39 < z < 2.30$. Nine of our [Ne V]-detected

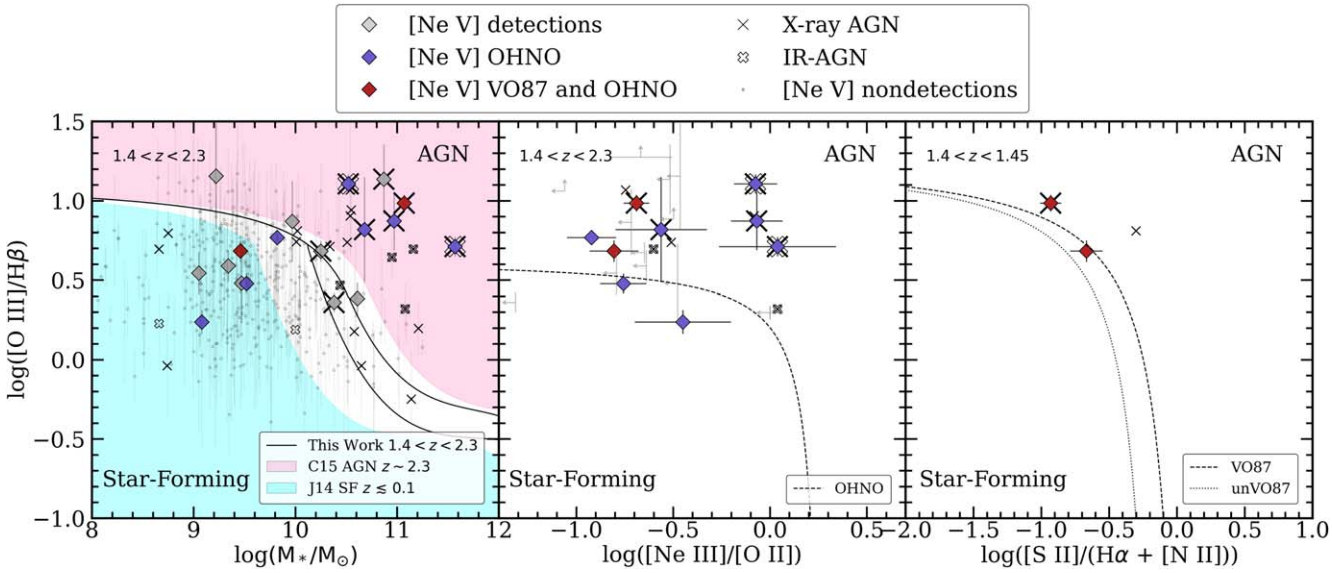


**Figure 4.** Emission-line diagnostics of star formation/AGN activity. Each panel requires S/N > 1 for all represented emission lines. Galaxies that lie above the respective dividing line are classified as AGNs, and galaxies that lie below the line are classified as star-forming. X-ray AGNs are shown with a thin cross, and IR AGNs are shows with a hollow cross. [Ne V]-detected objects are colored by their detected emission-line pairs: gray diamonds have detections in [O III]/Hβ only, dark-purple diamonds have [O III]/Hβ and [Ne III]/[O II] (OHNO), and red diamonds have [O III]/Hβ and [S II]/[Hα + [N II]] (VO87). Redshift ranges for the coverage of all respective lines are shown in the upper left corner of each panel. Left: MEx diagram—the relation of log([O III]/Hβ) vs. stellar mass. Galaxies in CLEAR that are undetected in [Ne V] in this redshift range ([Ne V] nondetections) are shown as small gray points. The blue and pink shaded regions show the local Juneau et al. (2014) star-forming and $z \sim 2.3$ Coil et al. (2015) AGN regions, respectively. The $z \sim 1.6$ redshift-evolved MEx line from Equation (4) is shown in black. Middle: the OHNO diagram using log([O III]/Hβ) vs. log([Ne III]/[O II]). We also show the limits of line ratios for objects in the cases where objects are undetected in various permutations of Hβ, [Ne III], or [O II]. Right: the VO87 diagram for log([O III]/Hβ) vs. log([S II]/[Hα + [N II]]). The dashed line shows the Veilleux & Osterbrock (1987) line for $z \sim 0$, and the dotted line shows the Backhaus et al. (2022) "unVO87" dividing line for galaxies at $z \sim 1$. The limited redshift range for the detection of all five of these lines leaves much smaller samples than other diagnostics. Both of the galaxies with VO87 lines also have detected [Ne III]/[O II]. Both the points with well-detected line ratios and limit behaviors of other [Ne V] detections suggest a broad preference for [Ne V] detections to be classified as AGNs in all three of these diagnostics. Based on these line diagnostic plots, the CLEAR [Ne V]-emitting galaxies are broadly consistent with ionization from AGNs.

objects are well detected in the four OHNO lines (using the OHNO AGN/star formation separation from Backhaus et al. 2022). Of these, eight (89%) have line ratios consistent with ionization of AGNs. This includes all five (100%) of the X-ray-detected [Ne V] sources in our sample. There is one galaxy in our [Ne V]-emitter sample that falls below the AGN line in the OHNO diagram, but it is consistent with being an AGN within its 1σ uncertainties based on the classification line defined by Backhaus et al. (2022). Therefore, for the [Ne V]-emitting galaxies in our sample that we can place on the OHNO diagram, all but one galaxy are 1σ consistent with ionization from AGNs. The single object that lies greater than 1σ outside of the AGN region of the OHNO diagram has large horizontal error bars owing to a low-S/N [O II] detection (we therefore cannot rule out ionization from an AGN in this object).

In the OHNO panel, we also show the limiting cases for objects in our sample that do not have well-detected Hβ, [Ne III], or [O II] emission lines, in various different permutations of undetected lines (i.e., those not detected in Hβ, [Ne III], [O II], or some combination thereof). This analysis shows that even the [Ne V]-detected objects without all of the necessary lines preferentially lie in the AGN region.

### 3.3. The "unVO87" Diagram

Another diagnostic used to separate AGNs and star-forming galaxies is the relation between [O III]/Hβ and [S II] combined with Hα (Veilleux & Osterbrock 1987, hereafter VO87). The VO87 diagram has been applied to many studies of galaxies (including AGNs and star formation) at $z \sim 0$ (Veilleux & Osterbrock 1987; Kewley et al. 2001; Kauffmann et al. 2003; Trump et al. 2015; Kewley et al. 2019a). The original VO87 relation to divide AGNs and star formation is given by

$$\log\left(\frac{[\mathrm{O\ III}]}{\mathrm{H}\beta}\right) = \frac{0.48}{\log([\mathrm{S\ II}]/\mathrm{H}\alpha) + 0.10} + 1.3. \quad (5)$$

At the resolution of the HST/WFC3 grisms, the [S II] lines are blended with each other, and Hα is blended with [N II]. We therefore use the "unresolved" VO87 relation (henceforth "unVO87"), which has been tested at $z \sim 1$ for galaxies where these lines are blended (unresolved; see Backhaus et al. 2022). In this case, Backhaus et al. (2022) define an empirically derived relation to separate AGNs and star-forming galaxies as follows:

$$\log\left(\frac{[\mathrm{O\ III}]}{\mathrm{H}\beta}\right) = \frac{0.48}{\log(\mathrm{S\ II}/[\mathrm{H}\alpha + \mathrm{N\ II}]) + 0.12} + 1.3, \quad (6)$$

where galaxies lying above the curve (higher [O III]/Hβ) are classified as AGNs and those below the curve are classified as star-forming for both the Veilleux & Osterbrock (1987) and Backhaus et al. (2022) curves.

Figure 4 (right panel) shows the unVO87 diagram for objects in CLEAR in the (rather) narrow redshift range that allows for HST G102 and G141 grism coverage of [Ne V] along with all of [O III], Hβ, [S II], and Hα ($1.39 < z < 1.45$). We show both the original $z \sim 0$ VO87 relation and the $z \sim 1$ unresolved unVO87 AGN/SF dividing lines. Given the very limited redshift range to allow for all four lines needed for unVO87 and [Ne V], there are only two [Ne V]-emitting objects in this

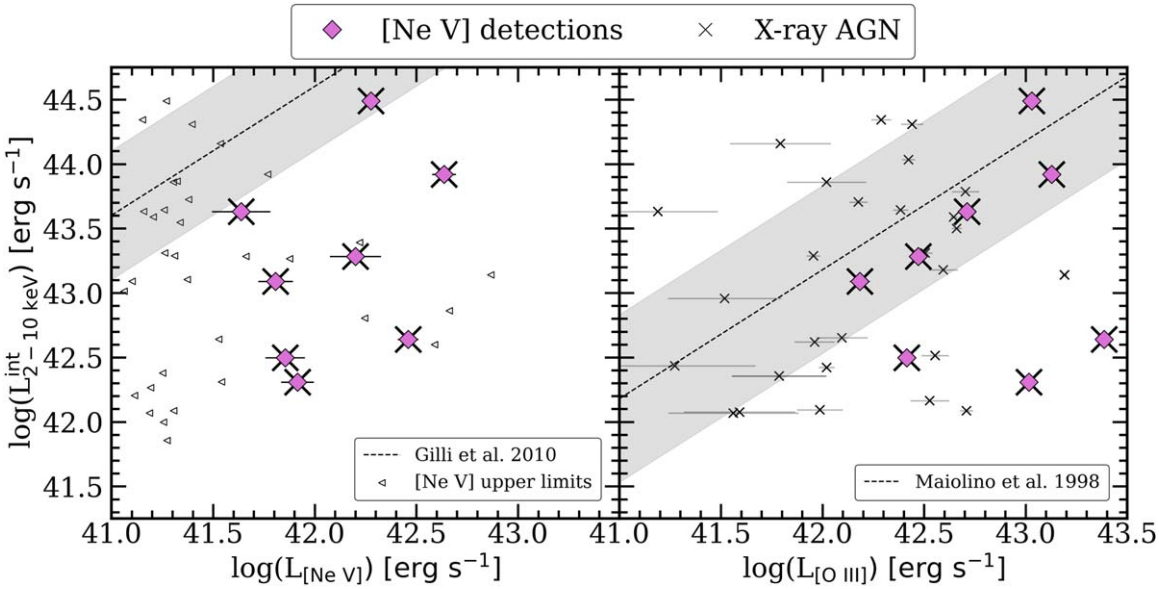


**Figure 5.** The relation between intrinsic X-ray luminosity and [Ne V] luminosity (left) and [O III] luminosity (right) for objects in CLEAR matching to the Xue et al. (2016) and Luo et al. (2017) X-ray catalogs, in the redshift range of our [Ne V] sample. [Ne V]-detected objects are shown as purple diamonds. We also show the $1\sigma$ upper limits for the [Ne V] nondetections as left-pointing black triangles. The black dashed lines and gray shaded regions in each panel show the median and $1\sigma$ relations for local Seyferts, respectively (Maiolino et al. 1998; Gilli et al. 2010). Our emission-line-selected sample has preferentially higher [Ne V] compared to X-ray luminosities than local Seyfert relations suggest.

subsample. These are shown in red. One of the [Ne V] detections in this panel is categorized as an X-ray AGN. The X-ray-undetected [Ne V] emitter is consistent with the unVO87 division within its uncertainties. There is also one object in the CLEAR sample that is undetected in [Ne V] in this redshift range, which is identified as an X-ray AGN and is classified as such by both the VO87 and unVO87 divisions.

As these emission-line ratio diagnostics suggest, the [Ne V] sources in CLEAR appear primarily consistent with ionization from AGNs. This is clear (pun intended) from the MEx diagram and the OHNO and VO87 relations in Figure 4, where the majority of the [Ne V] sources fall in regions consistent with ionization from AGNs. There are three objects that have contradictory classifications between the MEx and OHNO/VO87 diagnostics, but we favor the classifications from the emission-line diagnostics (OHNO and VO87), as they are not subject to the biases and uncertainties involved with the estimation of stellar masses from SED fitting. In total, all but 4 ($21/25 = 87.5\%$) of the [Ne V]-detected objects in our sample are consistent with AGN classification from these three diagnostics, either by their detected line ratios or by their limiting behaviors. We discuss the implications of the results of these analyses in Section 5.

## 4. Using X-Ray Emission to Characterize [Ne V]-emitting AGNs

In this section, we investigate the properties of [Ne V]-emitting galaxies in relation to their X-ray emission. We explore the use of observed [Ne V] $\lambda$3426 luminosities to probe AGN activity missed by other AGN selection methods, such as X-ray, IR, and emission-line diagnostics.

For the following analysis, we use luminosities of both X-ray detections and upper limits in X-rays for galaxies that are undetected ("X-ray nondetections"). We take X-ray fluxes from the CDF-N and CDF-S catalogs (Xue et al. 2016 and Luo et al. 2017, respectively). We calculate the upper limits of the luminosity of the X-ray nondetections using the hard-band flux detection limits from Xue et al. (2016) and Luo et al. (2017) of $5.9 \times 10^{-17}$ erg s$^{-1}$ cm$^{-2}$ and $2.7 \times 10^{-17}$ erg s$^{-1}$ cm$^{-2}$, respectively, and the grism redshifts from the CLEAR catalog. We perform a *K*-correction assuming a typical effective photon index of 1.8 (Yang et al. 2016; Liu et al. 2017). We transform our 0.5–7 keV luminosities to 2–10 keV luminosities for comparisons with other samples following Yang et al. (2016), where $L_{2-10\ keV} = 0.721 L_{0.5-7\ keV}$.

In Figure 5 we present the intrinsic X-ray luminosities for the eight [Ne V]-emitting galaxies classified as X-ray AGNs by the Xue et al. (2016) and Luo et al. (2017) CDF catalogs, in relation to the [Ne V] and [O III] luminosities. In the left panel, we also show the $1\sigma$ upper limits of the [Ne V] luminosity for X-ray AGNs in the CDF catalogs not detected in [Ne V]. We show the local Seyfert X-ray vs [Ne V] and [O III] luminosity relations from Gilli et al. (2010) and Maiolino et al. (1998), respectively.

Our first result is that the majority of the CLEAR [Ne V]-emitter galaxies have [Ne V] luminosities that exceed the local scaling relation. Figure 5 shows that only two of the eight [Ne V]-detected X-ray AGNs are consistent (within $1\sigma$) with the [Ne V]–X-ray relation of Gilli et al. (2010) (which was derived from the observed 2–10 keV luminosities from local Seyferts). However, five of the eight are consistent with the local [O III]–X-ray relation (derived from local Seyferts; Maiolino et al. 1998). We do not find anything that differentiates the three galaxies that are outliers on both the [Ne V]–X-ray and [O III]–X-ray relations from the rest of the sample: these three galaxies show no special features in their properties or spectra. We therefore conclude that AGNs span a larger variation in [Ne V] and X-ray emission than suggested from local Seyfert samples.

Our sample is biased to high [Ne V] luminosities by selection, which may be in part responsible for this result. However, we note that there are several objects that are

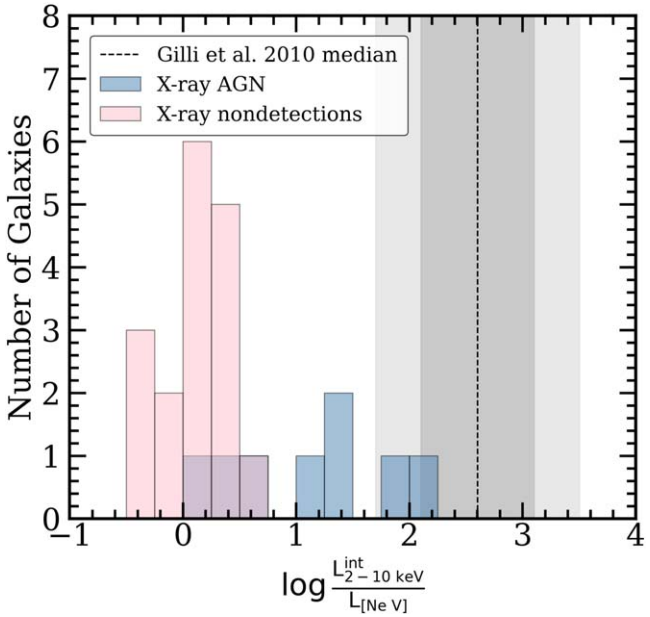


**Figure 6.** The distribution of the intrinsic X-ray/[Ne V] luminosity ratio for the eight X-ray-detected sources (blue) and upper limits for the 21 X-ray-nondetected sources (pink) in our [Ne V]-detected sample. The dashed black line and gray shaded regions show the median, $1\sigma$, and 90% ranges of the unobscured Seyferts in the Gilli et al. (2010) local sample. All but two objects in our sample lie below the 90% lower limits of the unobscured local Seyferts.

consistent with the local X-ray–[Ne V] and X-ray–[O III] relations.

If this result were due to an insufficient absorption correction to the observed X-ray luminosities, we would expect all of the objects from our sample to lie below the local relations. Instead, the large scatter in the X-ray luminosities of objects in our sample indicates that this is not the case: an additional flat correction needed to bring the low X-ray luminosity objects to the local relations would skew the objects with higher X-ray luminosities above the local relations. While a flat correction to all luminosities is likely not a perfect prescription, the objects that are discrepant from the local relations are uniformly distributed across all luminosities.

Previous studies have used the X-ray/[Ne V] luminosity ratio to study AGNs. Gilli et al. (2010) argued that the X-ray/[Ne V] luminosity ratio ($L_X/L_{[Ne\ V]}$) could be a useful indicator of CT AGNs. They observed that all Seyferts in their sample with $L_X/L_{[Ne\ V]} < 15$ showed evidence of CT AGNs. However, Gilli et al. (2010) assumed that AGNs have a near-constant intrinsic $L_X/L_{[Ne\ V]}$ ratio, in which case the lower observed $L_X/L_{[Ne\ V]}$ ratios imply obscuration of the X-ray emission.

Figure 6 shows the distribution of the X-ray/[Ne V] luminosity ratio for our sample, with the X-ray detections in blue and upper limits for the nondetections in pink. We also show the median ratio for the local ($z < 0.1$) Seyferts from Gilli et al. (2010). The gray shaded regions show the 68th and 90th percentiles for the Gilli et al. (2010) sample.

The X-ray/[Ne V] distribution for the CLEAR [Ne V]-emitter sample is systematically lower than that of the low-redshift Seyferts from Gilli et al. (2010). Only two of the objects in our CLEAR [Ne V]-emitter sample have $L_X/$[Ne V] ratios consistent (within the 90th percentile) with those of Gilli et al. (2010). The majority of the galaxies in our CLEAR [Ne V]-emitter sample—including four of the X-ray-detected galaxies and all 21 of the X-ray-nondetected galaxies—have X-ray/[Ne V] ratios below the canonical value of $L_X/$[Ne V] $< 15$ used to identify CT AGNs (Gilli et al. 2010). However, none of the [Ne V]-emitter galaxies in our sample are consistent with being CT AGNs given their absorption column densities (i.e., column densities $\log N_H < 24$; Li et al. 2019). Our sample has a range of column densities $21.45 < \log N_H < 23.95$. We therefore conclude that X-ray/[Ne V] does not uniquely identify CT AGNs.

One reason the X-ray/[Ne V] ratio is unable to identify CT AGNs may be because there are systematic differences in our CLEAR [Ne V]-emitter sample and other X-ray-selected samples of AGNs. In particular, our sample of high-redshift galaxies spans different luminosities and redshifts. Figure 7 shows the distribution of [Ne V] luminosities and intrinsic X-ray luminosities as a function of redshift for the eight galaxies in our [Ne V]-emitter sample detected in X-rays. The figure compares these to samples of lower-redshift ($z < 1.5$) luminous QSOs and very low redshift ($z < 0.1$) Seyferts (Gilli et al. 2010). For completeness, we include in the figure those galaxies in our CLEAR [Ne V] sample that are undetected in X-rays using the same prescription as those in Figure 6.

Figure 7 shows that the CLEAR [Ne V]–emitter sample has [Ne V] luminosities consistent with QSOs from $0 \lesssim z \lesssim 1$ but has X-ray luminosities that are much lower and more consistent with the range of X-ray luminosities seen in local Seyferts. This is evidence that there is greater variation between the X-ray engine in AGNs (presumably the accretion disk) and the NLR (which is responsible for the [Ne V] emission). We discuss this variation and its implications for the results of these analyses in Section 5.

## 5. Discussion

### 5.1. The Nature of [Ne V] Galaxies through Emission-line Ratio Diagnostics

The emission-line ratio diagnostics in Figure 4 have several implications for the nature of [Ne V]-emitting galaxies. In each of the three diagnostics (MEx, OHNO, and VO87), the [Ne V]-detected objects are consistent with ionization from AGNs: the MEx diagnostic classifies 12/18 (67%) [Ne V] detections as AGNs, while the more reliable, yet less inclusive, OHNO diagram classifies 8/9 (89%) [Ne V] detections as AGNs.

The presence of an AGN is expected given that the energy needed to produce [Ne V] is 97.11 eV. The ionizing spectra of stellar populations are not expected to produce copious radiation at this energy (Olivier et al. 2022). The presence of an AGN is supported by the fact that a large fraction (~32%) of the [Ne V] galaxies are detected in X-rays and/or selected as AGNs from their IR. This is especially true for the [Ne V] sources in the high-excitation (AGN) regions of the plots in Figure 4. Therefore, given the coincidence of AGNs among the [Ne V]-selected galaxies, AGNs appear to explain the origin of the [Ne V] emission in most of our sample here.

It is noteworthy, however, that there appears to be a population of [Ne V]-detected galaxies in CLEAR that have [O III]/H$\beta$ ratios below the threshold of traditional AGN selection. This includes six sources in the MEx diagram of Figure 4 with lower [O III]/H$\beta$ ($\lesssim$1), with lower stellar masses ($\log M_*/M_\odot < 10$), and that are undetected in the X-rays. While these objects have formally detected [Ne V] ($>3\sigma$), it is important to note that these six objects are among the weaker [Ne V] detections in our sample ($3 < S/N < 5$). To account for

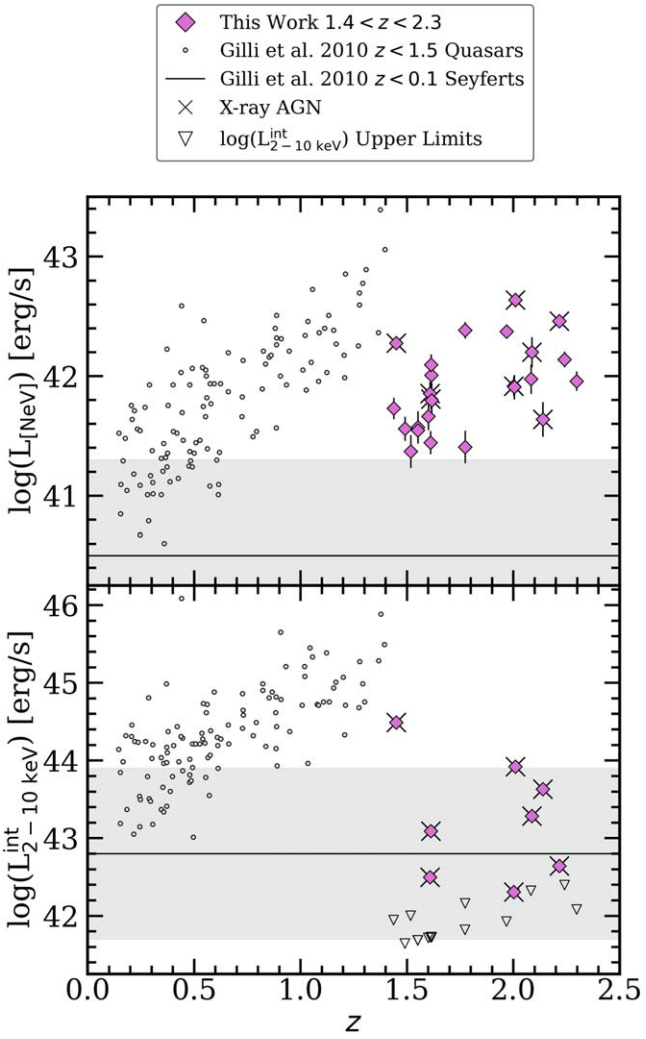


**Figure 7.** The relations of [Ne V] (top) and intrinsic X-ray (bottom) luminosity functions for the eight X-ray AGNs in our CLEAR sample (purple diamonds) and 112 lower-redshift QSOs ($z \lesssim 1.5$) from Gilli et al. (2010; gray circles). We also show the median of the X-ray and [Ne V] luminosities of the Gilli et al. (2010) local ($z < 0.1$) Seyfert sample as a black line, with the gray shaded region showing the $1\sigma$ scatter. We show $1\sigma$ uncertainties, which may be smaller than the size of the markers. Our higher-redshift [Ne V] selection probes a parameter space not observed in the X-ray-selected samples, with X-ray luminosities comparable to local Seyferts and higher [Ne V] luminosities more typical of $z \sim 1$ QSOs.

the [Ne V] emission in these galaxies requires some mechanism other than a bright AGN. This could include one or more of the following:

1. Heavily obscured AGNs: it is possible that these [Ne V] emitters contain deeply obscured AGNs such that the X-ray emission is undetectable (even in the 2 or 7 Ms depth data available for the CDF-N and CDF-S fields). Furthermore, obscured AGNs should be detected as IR AGNs (Donley et al. 2012), where, again, the CDF-N and CDF-S fields have some of the deepest far-IR imaging on the sky (Guo et al. 2013; Barro et al. 2019, and references therein). The lack of indications of AGN activity in the X-rays or IR emission in these galaxies disfavors this interpretation.
2. Weak AGNs: the [Ne V] emission could stem from weak AGNs, where again such objects would have X-ray emission below the detection limit for our sample. This is an intriguing possibility, especially given the lower stellar masses for these galaxies. It is possible that they host (lower-mass) intermediate-mass black holes with lower accretion rates but are still able to produce a strong NLR (Greene et al. 2020). Additional study of these galaxies for other high-ionization emission lines will be able to confirm this possibility (e.g., with rest-frame optical/near-IR spectroscopy from JWST). A related potential explanation for the low observed [O III]/H$\beta$ ratios in these objects is through star formation coincident with the AGN phase boosting the H$\beta$ fluxes, thus hiding the AGN activity given these typical diagnostics.
3. Shocks or other extreme mechanisms: [Ne V] emission has been detected in several low-mass, nearby galaxies, where those studies argue that the emission is produced by energetic shocks from supernovae or extreme stellar populations in a lower-metallicity, high-density ISM (Thuan & Izotov 2005; Izotov et al. 2012, 2021; Olivier et al. 2022). Leung et al. (2021) also find that [Ne V] may be produced in higher-metallicity objects that have (in at least one case) indications of shocked gas from AGN-driven winds. It is plausible that some of the [Ne V] emission in the lower-mass galaxies in our sample stems from similarly produced shocks. For this to be the case, we would expect to see indications of high density, which could be traced by resolved [S II] or other density-sensitive lines (see Figures 8 and 9 in Appendix A). Currently the HST/WFC3 grism data have insufficient resolution to study these lines at these redshifts, but this would be possible with future JWST spectroscopy at higher spectral resolution.

### 5.2. The Nature of [Ne V] Galaxies via Their X-Ray Emission

The study of [Ne V] in conjunction with observed-frame 2–10 keV luminosities offers insight into the relative amount of emission in the "hard UV"/"soft X-ray" regime (energies around ~100 eV) in the spectra of these galaxies. The [Ne V] emission therefore provides information unavailable from studies of AGN using only X-ray or IR. As noted above (in Figure 7), our sample of [Ne V]-emitter galaxies in CLEAR has [Ne V] emission similar to $z \sim 1$ QSOs but X-ray luminosities similar to local Seyferts. This means that the galaxies in our [Ne V]-emitter sample have a lower X-ray/[Ne V] luminosity ratio than seen in other samples. We discuss here our interpretation of the conditions for the lower X-ray/[Ne V] ratios. Specifically, this must be a result of (1) reduced X-ray emission and/or (2) enhanced [Ne V] emission in these higher-redshift objects.

The preferentially low X-ray/[Ne V] ratios of our sample suggest an excess of ~0.1 keV photons compared to the emission at >1 keV emission. Enhanced [Ne V] emission could be caused by several effects (or a combination of effects). Strictly speaking, it requires a higher density of ~100 eV photons. This could result from different geometry of the NLR and accretion disk (Trump et al. 2011), or conditions that conspire to enhance the emission of these "soft X-ray" photons compared to the ionizing spectrum of local objects. This could also be a result of excess [Ne V] from shocked gas from AGN winds (Leung et al. 2021).

If geometry is the culprit of the enhanced [Ne V] emission, then specific conditions seem to be required. For example, the enhanced [Ne V] could be explained by anisotropy in the X-ray emission (Yang et al. 2020) such that the NLR is illuminated by the accretion disk but the sight line to the central engine is obscured. However, this obscuration would likely be seen in the X-ray absorbing column, where the absorption column densities, $N_{\rm H}$, of our sample suggest that our objects are not CT (i.e., $\log N_{\rm H} < 24$; Li et al. 2019). As such, we conclude that the sources in our [Ne V]-selected sample are not CT, in spite of their very low X-ray/[Ne V] ratios. This contrasts with findings presented in Gilli et al. (2010) and Mignoli et al. (2013), who argued that low X-ray/[Ne V] emission in type 1 Seyferts and QSOs should be indicative of CT AGNs.[21] It therefore seems unlikely that viewing angle combined with anisotropic emission can by itself explain the enhanced [Ne V] in our sample. However, we note that there is an important difference in the selection methods of our sample and those of the Gilli et al. (2010) and Mignoli et al. (2013) samples, where those works are at lower redshift than this work and have shallower X-ray data (100–200 ks) than the Chandra Deep Fields (2–7 Ms). These selection effects will lead to higher X-ray/[Ne V] ratios in Gilli et al. (2010) and Mignoli et al. (2013), as these samples will be insensitive to lower X-ray luminosities, e.g., the sample in Mignoli et al. (2013) reaches a flux limit of $7.3 \times 10^{-16}$ erg s$^{-1}$cm$^{-2}$, where the CDF catalogs reach an order of magnitude fainter ($2.7 \times 10^{-17}$ erg s$^{-1}$cm$^{-2}$ in CDF-S). These differences in sample selection may account for some of the X-ray/[Ne V] ratio discrepancies found in this work. It will be informative to study these potential selection biases in both samples with future studies of larger samples of [Ne V]-detected objects in deep X-ray surveys.

It is still possible that the geometry of the accretion disk itself is able to produce the conditions for enhanced [Ne V] emission. This could result from an AGN with an excess of emission from the inner disk (to produce the soft X-ray photons) but less coronal emission. If the latter case applies to the galaxies in our sample of [Ne V] galaxies, then it predicts that we should observe SEDs with exceptionally bright UV and soft X-rays (i.e., a prominent soft X-ray excess; see, e.g., Done et al. 2012). We may test this in future work with rest-frame far-UV spectroscopy of these galaxies to more precisely constrain their hard UV/soft X-ray spectra.

The geometry may also manifest itself in the form of absorption from a warm wind. AGNs with a "soft excess" (of X-ray photons around 0.1 keV) have been observed in samples of Seyferts and QSOs (Walter & Fink 1993). The origin of this emission is unclear, as the shape of the SED is not consistent with models of pure optically thin or thick accretion disks (Walter & Fink 1993; Gierliński & Done 2004). One explanation for the soft excess that is tied to the geometry is that the excess is an artifact of absorption of highly ionized atoms (e.g., O VI, O VII, and several iron species) in a warm, relativistic wind ejected from the accretion disk that preferentially absorbs ∼1 keV photons (Gierliński & Done 2004). The soft excess could provide the number density of ∼0.1 keV photons to power the [Ne V] emission in our sample. If this is the case, we would expect to possibly see a correlation between [Ne V] emission lines and broad absorption features in X-ray spectra, or with the spectral shape of the X-ray emission from ∼0.1 to 50 keV data. Currently these observations are beyond the sensitivity of X-ray telescopes.

Regardless, our results add evidence that there is a greater diversity and variation in the intrinsic X-ray/[Ne V] ratio given the complexities of the relationship between the NLR and X-ray emission. We will be able to explore these models more deeply with larger samples from Nancy Grace Roman Space Telescope and greater wavelength coverage from JWST. A full suite of UV/optical emission features in conjunction with mid-IR photometry will give a more complete picture of the physical mechanisms of these extreme high-ionization systems, and with coverage to much higher redshifts ($6 < z < 11$ with JWST/NIRCam and NIRSpec).

## 6. Summary and Conclusions

In this work, we used HST G102 and G141 grism observations to study a sample of 25 galaxies in the CLEAR survey displaying significant [Ne V] $\lambda$3426 emission at redshift $1.40 < z < 2.29$. We consider these objects of interest owing to the extremely high energy (97.11 eV) required to create [Ne V] compared to other strong UV/optical emission lines. Our sample selection required S/N > 3 of the stronger [Ne V] line ($\lambda$3426) and [O III] and minimal contamination in the 1D and 2D spectra by visual inspection.

The primary findings of this work are as follows:

1. Galaxies with [Ne V] detections are much more likely to be X-ray AGNs than the general population of galaxies in the CLEAR survey. We cross-matched our sample of [Ne V]-emitting galaxies in CLEAR with the deep (2 and 7 Ms) catalogs from the Chandra X-ray Observatory from Luo et al. (2017) and Xue et al. (2016). We find that about one-third (32%, 8/25) of the [Ne V]-detected objects in our sample are X-ray-detected AGNs, compared to 6.5% of the galaxies in the mass- and redshift-matched CLEAR parent sample that are undetected in [Ne V].
2. We use optical emission-line ratios (based primarily on [O III]/H$\beta$) to study the ionization of the [Ne V]-emitting galaxies. The three spectral classifications include the MEx, "OHNO," and "unVO87" diagrams, which are shown in Figure 4. They show that most of the [Ne V] emitters are consistent with ionization with AGNs, with the most reliable of these (OHNO) classifying 89% of [Ne V] galaxies as AGNs. This is particularly true for X-ray-detected [Ne V] sources, where all X-ray and [Ne V] sources are consistent with AGNs. In this work, we also include an updated redshift dependence of the MEx diagnostic, which we quantify in Equation (4) as a shift in mass from the local Juneau et al. (2014) relation.
3. There are several [Ne V]-emitting galaxies that are not classified as AGNs by X-ray or IR emission or by emission-line ratio diagnostics in Figure 4. These are mostly at lower stellar masses ($\log M_*/M_\odot < 10$), suggesting that [Ne V] selections probe AGNs at intermediate mass scales or that other highly energetic photoionization mechanisms or shocks are driving the line emission.
4. We explore (and reject) the possibility that the [Ne V] emitters in our sample are produced by heavily obscured AGNs by studying the X-ray/[Ne V] luminosity ratio. We find that the X-ray/[Ne V] emission for our X-ray-

[21] It may be that CT AGNs have low X-ray/[Ne V] ratios, as argued by Gilli et al. (2010) and Mignoli et al. (2013). However, the X-ray/[Ne V] ratios of the [Ne V] galaxies in our CLEAR sample imply that low X-ray/[Ne V] ratios would then be a necessary but not sufficient condition for CT AGNs.

detected [Ne V] emitters (and upper limits for galaxies undetected in X-rays) cannot be used to diagnose CT AGNs for our objects. The hydrogen absorption column densities for our objects from Li et al. (2019) support that objects in our sample are not in the CT regime $\log N_{\rm H} > 24$. The use of the X-ray/[Ne V] ratio to select CT AGNs seems restricted to more luminous objects, such as X-ray-selected QSOs and unobscured (type 1) Seyferts, which have much higher intrinsic X-ray luminosities than our [Ne V]-selected sample.

5. We argue that the [Ne V] emission in our sample provides evidence for increased variation and diversity in the nature of the accretion disk and NLR of AGNs at $z > 1$. To account for the enhanced [Ne V] requires an excess of "soft X-ray" / "hard UV" photons (at energies around ~0.1 keV, the creation energy of [Ne V]). This could be related to the "soft excess" seen in the spectra of other QSOs and AGNs. It could also be related to changes in the geometry, or possibly from absorption of moderately ionized gas in a relativistic wind blown off from the accretion disk. These models can be tested by studying the SED of the X-ray emission and/or by studying additional line ratios to better trace the ionizing spectrum, which should be possible with studies from, e.g., JWST.

Our results show that [Ne V] emission probes highly energetic photoionization (~100 eV). We attribute [Ne V] production predominantly to AGN activity, and we use [Ne V] to probe AGNs missed by other methods (X-ray and IR). Other potential creation mechanisms not explored in this work, which will be explored in future studies, include energetic shocks from supernovae and extreme ionizing stellar populations.

Our results motivate future observations of [Ne V] emission to measure the excitation of galaxies within a much larger redshift range, including the EoR ($z \gtrsim 6$). The James Webb Space Telescope (JWST) will reach a flux limit that is an order of magnitude fainter than our CLEAR data for similar exposure times, enabling detection of fainter [Ne V] line emission. JWST/MIRI will be particularly beneficial in the detection of 15–30 $\mu$m emission from the AGNs in our sample to resolve the geometry of the X-ray anisotropy. JWST is outfitted with NIRSpec and NIRCam, which will give both slit and slitless spectroscopy covering strong UV high-ionization emission lines, like the [Ne V] doublet, at $0.8 < z < 14.4$. JWST/NIRISS will also give slitless coverage of [Ne V] at slightly lower redshift ranges ($3 < z < 7$).

The Nancy Grace Roman Space Telescope will also be able to study the spectra of high-ionization systems in samples orders of magnitude larger than any previous work. With the Wide Field Instrument (WFI), Roman will give low-resolution ($R \sim 600$) multiobject slitless grism spectroscopy with wavelength coverage 1–1.93 $\mu$m, similar to that of HST/WFC3 G102+G141 but with a field of view two orders of magnitude larger in area.

Lastly, we note that first-look JWST/NIRSpec spectra have already shown strong detections of UV and optical spectral features in this redshift range (Brinchmann 2022; Katz et al. 2022; Trump et al. 2022; Cleri et al. 2023). Early results show great promise that this new generation of spectroscopic data will give critical insight into the nature of galaxies in the early universe and may decisively answer questions about the key contributors to the EoR.

The authors wish to thank our colleagues in the CLEAR collaboration for their work on this project and their assistance and support. N.J.C. also thanks Maeve Curliss for significant discussion on the data visualization in this work. N.J.C. also thanks Justin Spilker (Justin with the PhD) and Justin Cole (Justin without the PhD) for insightful discussions throughout the course of this work. N.J.C. also acknowledges the rejected acronym for AGNs exhibiting strong UV/optical features with X-ray emission weaker/comparable to local Seyferts (Strong UV/Optical emission-line, Normal X-ray (STONX) AGNs).

This work is based on data obtained from the Hubble Space Telescope through program No. GO-14227. Support for program No. GO-14227 was provided by NASA through a grant from the Space Telescope Science Institute, which is operated by the Association of Universities for Research in Astronomy, Incorporated, under NASA contract NAS5-26555. N.J.C., J.R.T., and B.E.B. acknowledge support from NSF grant CAREER-1945546 and NASA grants JWST-ERS-01345 and 18-2ADAP18-0177. N.J.C. and C.P. also acknowledge support from NASA/HST AR 16609. This work acknowledges support from the NASA/ESA/CSA James Webb Space Telescope through the Space Telescope Science Institute, which is operated by the Association of Universities for Research in Astronomy, Incorporated, under NASA contract NAS5-03127. Support for program No. JWST-ERS01345 was provided through a grant from the STScI under NASA contract NAS5-03127.

*Software:* `grizli` (Brammer et al. 2008), FAST (Kriek et al. 2009), EAZY (Brammer et al. 2008; Wuyts et al. 2011), Astropy (Astropy Collaboration et al. 2013), NumPy Harris et al. 2020, Matplotlib (Hunter 2007), `PyNeb` (Luridiana et al. 2015), seaborn (Waskom 2021), pandas (Reback et al. 2022).

## Appendix A
## Comparisons with Photoionization Models

In this appendix, we present photoionization models of the emissivities of several of the spectral features of importance in this work. We employ the `PyNeb` photoionization modeling code (Luridiana et al. 2015). `PyNeb` does not invoke a particular ionizing spectrum, instead modeling the emissivity of each species from an ionized gas regardless of the initial conditions of said gas.

Given the relatively low spectral resolution of the G102 and G141 grisms, several of the emission lines are unresolved. We define the [Ne III]/[O II] (Ne3O2) in terms of the coadded [O II] doublet

$$\frac{[\text{Ne III}]}{[\text{O II}]} \equiv \frac{[\text{Ne III}]\ \lambda 3869}{[\text{O II}]\ \lambda\lambda 3726,\ 3729} \tag{A1}$$

and the [O III]/[O II] ratio (O32) in terms of the coadded [O III] and [O II] doublets

$$\text{O}_{32} \equiv \frac{[\text{O III}]\ \lambda\lambda 4959,\ 5007}{[\text{O II}]\ \lambda\lambda 3726,\ 3729}. \tag{A2}$$

In Figure 8 we show emissivity maps as a function of temperature and density for several relevant emission features of neon and oxygen ([Ne V] $\lambda\lambda$3426 and 3346, [Ne III] $\lambda$3869, [O III] $\lambda\lambda$5007 and 4959, and [O II] $\lambda\lambda$3726 and 3729). We also show the coadded [O III] $\lambda\lambda$4959,5007 and [O II] $\lambda\lambda$3726, 3729 doublets. We note that the neon line emissivities do not significantly evolve with density and do evolve with

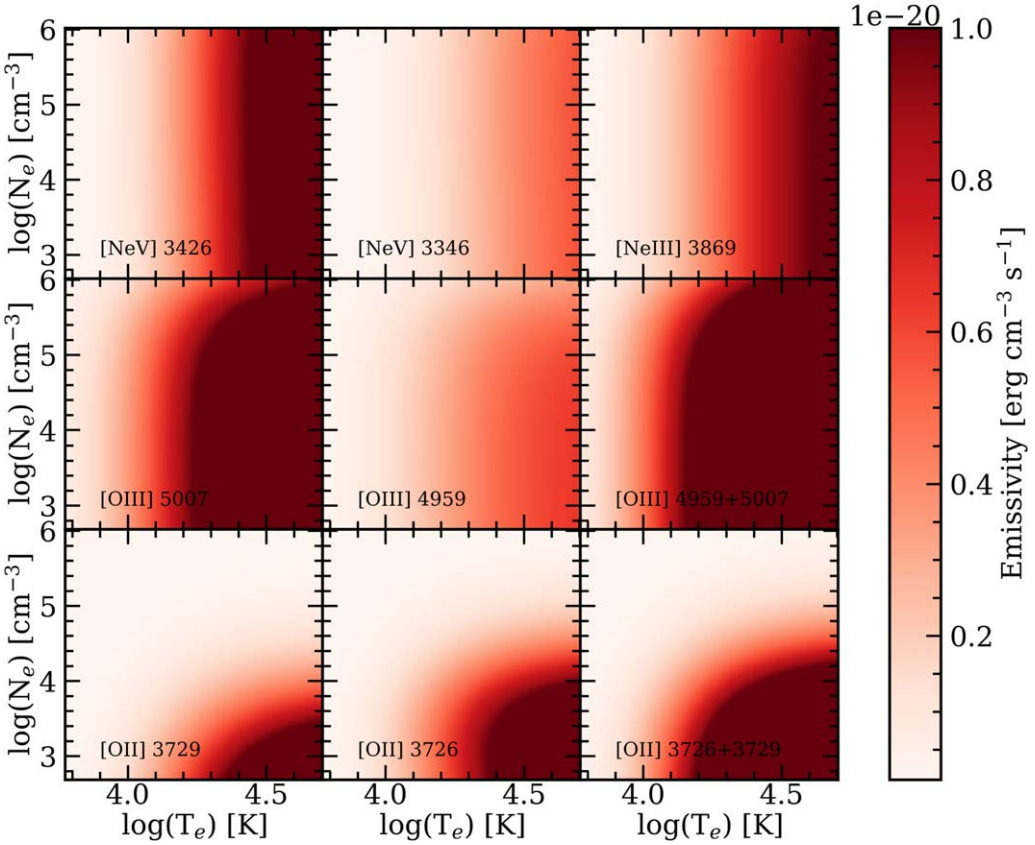


**Figure 8.** PyNeb models for several relevant emission-line emissivities as a function of temperature and density. The emissivities are all given on the same color map scale. We see that the neon species shown here ([Ne V] and [Ne III]) evolve only with temperature, while the oxygen species have evolution with both temperature and density in this parameter space. Given the spectral resolution of the HST/WFC3 grisms, we also show the coadded [O II] and [O III] emission grids.

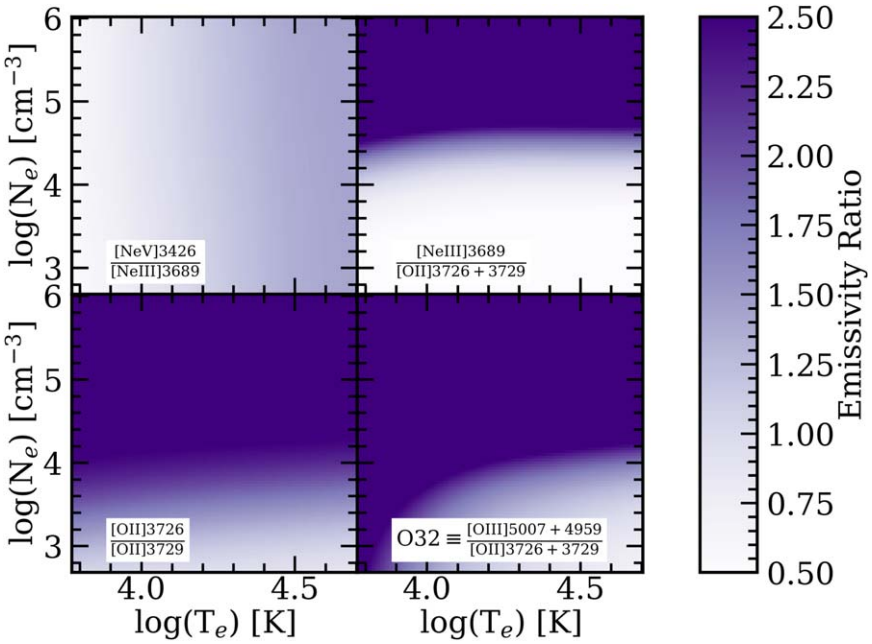


**Figure 9.** PyNeb models for several relevant emission-line ratios as a function of temperature and density. The ratio of the individual features of the [Ne V] and [O III] doublets are constant in this temperature and density parameter space, and their constant ratios are given (2.73 and 2.98, respectively). The [Ne V]/[Ne III] ratio is an indicator of temperature, where [O II]/[O II] and [Ne III]/[O II] ratios are primarily functions of density.

temperature. The oxygen lines evolve with both temperature and density.

In Figure 9 we show ratios of emissivities of several of the emission lines from Figure 8 computed from PyNeb. The [Ne V] $\lambda$3426/[Ne V] $\lambda$3346 and [O III] $\lambda$5007/[O III] $\lambda$4959 ratios are both constant with temperature and density with values 2.73 and 2.98, respectively. We see that the [Ne V] $\lambda$3426/[Ne III] $\lambda$3869 ratio increases with temperature. The

[Ne III]/[O II] ratio evolves primarily with density within this parameter space.

We also show the [O II] $\lambda$3726/[O II] $\lambda$3729 ratio, which increases solely as a function of density in this parameter space. The [Ne III]/[O II] and O32 ratios, as defined by Equations (A1) and (A2), respectively, vary with both temperature and density.

## Appendix B
## Sample Characteristics, Derived Quantities, and Emission-line Fluxes

In this appendix, we present the sample characteristics and derived quantities (Table 1) and the emission-line fluxes for relevant lines used in this work (Table 2).

**Table 1**
Sample Characteristics and Derived Quantities

| Field | 3D-HST ID | R.A. (deg) | Decl. (deg) | Redshift[a] | Stellar Mass[b] $\log(M_*/M_\odot)$ | $SFR_{UV}^{corr}$[c] ($M_\odot$ yr$^{-1}$) | F435W−F775W[c] |
|---|---|---|---|---|---|---|---|
| GN | 11743 | 189.2213 | 62.2002 | 2.0834 | 9.22 | 10.8 ± 0.9 | 0.26 ± 0.07 |
| GN | 19464 | 189.0871 | 62.2376 | 2.0877 | 10.97 | 250 ± 10 | 1.0 ± 0.1 |
| GN | 19591 | 189.2013 | 62.2380 | 2.002 | 10.25 | 260 ± 2 | 0.52 ± 0.03 |
| GN | 19913 | 189.1483 | 62.2400 | 2.0104 | 11.57 | 1100 ± 40 | 0.84 ± 0.03 |
| GN | 21290 | 189.2681 | 62.2462 | 2.2165 | 10.52 | 365 ± 3 | 0.05 ± 0.07 |
| GN | 21412 | 189.1749 | 62.2476 | 2.0051 | 9.47 | 9.9 ± 0.2 | 0.51 ± 0.10 |
| GN | 24427 | 189.3708 | 62.2617 | 1.7744 | 9.82 | 190 ± 10 | 0.30 ± 0.02 |
| GS | 24803 | 53.1613 | −27.7958 | 1.4913 | 9.46 | 9.0 ± 0.7 | 0.49 |
| GS | 26021 | 53.1604 | −27.7904 | 1.6117 | 9.52 | 12 ± 1 | 0.10 |
| GS | 28218 | 53.1469 | −27.7818 | 1.5516 | 9.05 | 4.0 ± 0.4 | 0.28 |
| GS | 29293 | 53.1583 | −27.7774 | 1.5523 | 8.87 | 3.89 ± 0.02 | -0.04 |
| GN | 37738 | 189.2812 | 62.3633 | 1.4506 | 11.07 | 106 ± 2 | 0.48 ± 0.02 |
| GN | 37767 | 189.2960 | 62.3628 | 1.5181 | 9.08 | 7.2 ± 0.3 | 0.21 ± 0.09 |
| GS | 38636 | 53.1269 | −27.7302 | 1.601 | 9.05 | 6.2 ± 0.7 | 0.05 |
| GS | 40305 | 53.1228 | −27.7228 | 1.6132 | 10.68 | 70 ± 2 | 0.83 |
| GS | 41195 | 53.1653 | −27.7185 | 1.9687 | 9.97 | … | 0.31 |
| GS | 41886 | 53.0977 | −27.7153 | 2.1397 | 10.87 | 183 ± 9 | 0.91 |
| GS | 42614 | 53.0923 | −27.7122 | 1.6149 | 10.05 | 12 ± 2 | 0.34 |
| GS | 42758 | 53.1122 | −27.7110 | 1.6085 | 10.38 | 1500 ± 900 | 0.71 |
| GS | 44556 | 53.1081 | −27.7020 | 1.7736 | 9.34 | 6 ± 1 | 0.22 |
| GS | 44783 | 53.1136 | −27.7014 | 1.6145 | 10.61 | 320 ± 10 | 0.78 |
| GS | 45337 | 53.1117 | −27.699 | 1.6173 | 9.95 | 60 ± 1 | 0.19 |

**Notes.**
[a] Grism redshifts from CLEAR (Simons et al. 2023).
[b] From the 3D-HST catalog (Skelton et al. 2014). Masses have characteristic uncertainty of 0.3 dex.
[c] From the CANDELS/SHARDS catalog (Barro et al. 2019). Objects without uncertainties on photometry are nondetections in both filters.

**Table 2**
Observed Emission-line Fluxes from CLEAR ($10^{-17}$ erg s$^{-1}$cm$^{-2}$; Simons et al. 2023)

| Field | ID | [Ne *v*] $\lambda$3426 | [O II] $\lambda\lambda$3726, 3729 | $\lambda$3869 | H$\beta$ | [O III] $\lambda\lambda$4959, 5007 | H$\alpha$+[N II] $\lambda\lambda$6548, 6583 | [S II] $\lambda\lambda$6717, 6731 |
|---|---|---|---|---|---|---|---|---|
| GN | 11743 | 2.83 ± 0.8 | 2.04 ± 0.78 | … | 0.69 ± 0.53 | 9.84 ± 0.6 | … | |
| GN | 19464 | 4.73 ± 1.37 | 4.54 ± 0.84 | 3.87 ± 0.95 | 1.19 ± 0.5 | 8.84 ± 0.55 | … | … |
| GN | 19913 | 14.16 ± 1.92 | 4.81 ± 1.69 | 5.26 ± 3.16 | 8.56 ± 1.18 | 44.01 ± 1.41 | … | … |
| GN | 21290 | 7.42 ± 0.87 | 7.11 ± 0.98 | 5.98 ± 1.3 | 4.91 ± 0.67 | 62.73 ± 0.96 | … | … |
| GN | 21412 | 2.66 ± 0.63 | 2.1 ± 0.58 | 0.4 ± 0.95 | 1.24 ± 0.67 | 3.73 ± 0.74 | … | … |
| GN | 24192 | 3.45 ± 0.53 | 3.12 ± 0.71 | … | 3.3 ± 0.48 | 15.55 ± 0.64 | … | … |
| GN | 24427 | 10.76 ± 1.7 | 45.19 ± 1.43 | 5.42 ± 1.57 | 24.0 ± 1.05 | 140.77 ± 1.47 | … | … |
| GS | 24803 | 2.48 ± 0.58 | 7.73 ± 0.4 | 1.21 ± 0.35 | 3.17 ± 0.49 | 15.3 ± 0.51 | 11.38 ± 0.39 | 2.45 ± 0.67 |
| GS | 26021 | 1.57 ± 0.35 | 5.6 ± 0.24 | 0.98 ± 0.27 | 2.71 ± 0.36 | 8.14 ± 0.4 | 15.85 ± 4.08 | |
| GN | 28055 | 4.02 ± 0.84 | … | … | 4.04 ± 0.35 | 8.02 ± 0.38 | … | … |
| GS | 28218 | 2.31 ± 0.72 | 2.2 ± 0.52 | … | … | 5.38 ± 0.6 | 4.73 ± 0.78 | … |
| GS | 29293 | 2.17 ± 0.49 | 4.53 ± 0.33 | 0.97 ± 0.36 | 0.37 ± 0.42 | 13.21 ± 0.45 | 6.66 ± 0.65 | |
| GN | 37738 | 13.86 ± 1.36 | 22.77 ± 0.79 | 4.65 ± 0.69 | 8.13 ± 0.99 | 78.6 ± 1.38 | 47.53 ± 1.08 | 5.57 ± 1.0 |
| GN | 37767 | 1.53 ± 0.48 | 1.51 ± 0.32 | 0.54 ± 0.29 | 3.23 ± 0.46 | 5.6 ± 0.53 | … | … |
| GS | 38636 | 2.64 ± 0.69 | 4.34 ± 0.58 | … | 2.51 ± 0.74 | 8.78 ± 0.77 | … | … |
| GS | 40305 | 3.61 ± 0.71 | 3.59 ± 0.51 | 0.98 ± 0.52 | 1.3 ± 0.98 | 8.58 ± 1.0 | 18.92 ± 8.11 | … |
| GS | 41195 | 8.13 ± 1.12 | 29.22 ± 1.16 | … | 3.47 ± 2.01 | 25.76 ± 2.21 | … | … |
| GS | 41218 | 2.14 ± 0.4 | 3.64 ± 0.87 | … | 1.53 ± 0.72 | 11.2 ± 0.85 | … | … |
| GS | 41886 | 1.22 ± 0.4 | 2.29 ± 0.83 | … | 1.06 ± 0.53 | 14.46 ± 0.64 | … | … |
| GS | 42614 | 5.71 ± 1.19 | 8.03 ± 0.82 | … | | 8.09 ± 1.64 | 43.89 ± 8.87 | … |
| GS | 42758 | 4.06 ± 0.91 | 14.43 ± 0.62 | … | 6.42 ± 0.83 | 14.73 ± 0.83 | 103.14 ± 10.23 | … |
| GS | 44556 | 1.14 ± 0.36 | 3.04 ± 0.3 | 0.01 ± 0.31 | 1.79 ± 0.39 | 6.93 ± 0.46 | … | … |
| GS | 44783 | 6.98 ± 1.41 | 26.31 ± 0.98 | … | 8.07 ± 1.72 | 19.59 ± 1.68 | 183.36 ± 20.2 | … |
| GS | 45337 | 3.49 ± 1.15 | 28.53 ± 0.83 | 3.14 ± 1.13 | … | 34.76 ± 1.79 | 21.95 ± 7.72 | … |

## ORCID iDs

Nikko J. Cleri https://orcid.org/0000-0001-7151-009X
Guang Yang https://orcid.org/0000-0001-8835-7722
Casey Papovich https://orcid.org/0000-0001-7503-8482
Jonathan R. Trump https://orcid.org/0000-0002-1410-0470
Bren E. Backhaus https://orcid.org/0000-0001-8534-7502
Vicente Estrada-Carpenter https://orcid.org/0000-0001-8489-2349
Steven L. Finkelstein https://orcid.org/0000-0001-8519-1130
Mauro Giavalisco https://orcid.org/0000-0002-7831-8751
Taylor A. Hutchison https://orcid.org/0000-0001-6251-4988
Zhiyuan Ji https://orcid.org/0000-0001-7673-2257
Intae Jung https://orcid.org/0000-0003-1187-4240
Jasleen Matharu https://orcid.org/0000-0002-7547-3385
Ivelina Momcheva https://orcid.org/0000-0003-1665-2073
Grace M. Olivier https://orcid.org/0000-0002-4606-4240
Raymond Simons https://orcid.org/0000-0002-6386-7299
Benjamin Weiner https://orcid.org/0000-0001-6065-7483

## References

Astropy Collaboration, Robitaille, T. P., Tollerud, E. J., et al. 2013, A&A, 558, A33
Backhaus, B. E., Bridge, J. S., Trump, J. R., et al. 2023, ApJ, 943, 37
Backhaus, B. E., Trump, J. R., Cleri, N. J., et al. 2022, ApJ, 926, 161
Barro, G., Pérez-González, P. G., Cava, A., et al. 2019, ApJS, 243, 22
Berg, D. A., Chisholm, J., Erb, D. K., et al. 2019, ApJL, 878, L3
Berg, D. A., Chisholm, J., Erb, D. K., et al. 2021, ApJ, 922, 170
Brammer, G. B., van Dokkum, P. G., & Coppi, P. 2008, ApJ, 686, 1503
Brinchmann, J. 2022, arXiv:2208.07467
Bruzual, G., & Charlot, S. 2003, MNRAS, 344, 1000
Chabrier, G. 2003, PASP, 115, 763
Cleri, N. J., Olivier, G. M., Hutchison, T. A., et al. 2023, arXiv:2301.07745
Cleri, N. J., Trump, J. R., Backhaus, B. E., et al. 2022, ApJ, 929, 3
Coil, A. L., Aird, J., Reddy, N., et al. 2015, ApJ, 801, 35
Done, C., Davis, S. W., Jin, C., Blaes, O., & Ward, M. 2012, MNRAS, 420, 1848
Donley, J. L., Koekemoer, A. M., Brusa, M., et al. 2012, ApJ, 748, 142
Erb, D. K., Shapley, A. E., Pettini, M., et al. 2006, ApJ, 644, 813
Estrada-Carpenter, V., Papovich, C., Momcheva, I., et al. 2019, ApJ, 870, 133
Estrada-Carpenter, V., Papovich, C., Momcheva, I., et al. 2020, ApJ, 898, 171
Fazio, G. G., Hora, J. L., Allen, L. E., et al. 2004, ApJS, 154, 10
Gierliński, M., & Done, C. 2004, MNRAS, 349, L7
Gilli, R., Vignali, C., Mignoli, M., et al. 2010, A&A, 519, A92
Greene, J. E., Strader, J., & Ho, L. C. 2020, ARA&A, 58, 257
Grogin, N. A., Kocevski, D. D., Faber, S. M., et al. 2011, ApJS, 197, 35
Guo, Y., Ferguson, H. C., Giavalisco, M., et al. 2013, ApJS, 207, 24
Harris, C. R., Millman, K. J., van der Walt, S. J., et al. 2020, Natur, 585, 357
Heckman, T. M., Ptak, A., Hornschemeier, A., & Kauffmann, G. 2005, ApJ, 634, 161
Hickox, R. C., & Alexander, D. M. 2018, ARA&A, 56, 625
Hunter, J. D. 2007, CSE, 9, 90
Izotov, Y. I., Thuan, T. X., & Guseva, N. G. 2021, MNRAS, 508, 2556
Izotov, Y. I., Thuan, T. X., & Privon, G. 2012, MNRAS, 427, 1229
Juneau, S., Bournaud, F., Charlot, S., et al. 2014, ApJ, 788, 88
Juneau, S., Dickinson, M., Alexander, D. M., & Salim, S. 2011, ApJ, 736, 104
Jung, I., Papovich, C., Finkelstein, S. L., et al. 2022, ApJ, 933, 87
Katz, H., Saxena, A., Cameron, A. J., et al. 2023, MNRAS, 518, 592
Kauffmann, G., Heckman, T. M., Tremonti, C., et al. 2003, MNRAS, 346, 1055
Kennicutt, R. C. J. 1998, ApJ, 498, 541
Kewley, L. J., Heisler, C. A., Dopita, M. A., & Lumsden, S. 2001, ApJS, 132, 37
Kewley, L. J., Nicholls, D. C., Sutherland, R., et al. 2019a, ApJ, 880, 16
Kewley, L. J., Nicholls, D. C., & Sutherland, R. S. 2019b, ARA&A, 57, 511
Koekemoer, A. M., Faber, S. M., Ferguson, H. C., et al. 2011, ApJS, 197, 36
Kriek, M., van Dokkum, P. G., Labbé, I., et al. 2009, ApJ, 700, 221
Lacy, M., Storrie-Lombardi, L. J., Sajina, A., et al. 2004, ApJS, 154, 166
Lambrides, E. L., Chiaberge, M., Heckman, T., et al. 2020, ApJ, 897, 160
Lee, J. C., Pirzkal, N., & Hilbert, B. 2014, Flux Calibration Monitoring: WFC3/IR G102 and G141 Grisms, Instrument Science Report WFC3 2014-01 STScI
Lehmer, B. D., Alexander, D. M., Bauer, F. E., et al. 2010, ApJ, 724, 559
Leung, G. C. K., Coil, A. L., Rupke, D. S. N., & Perrotta, S. 2021, ApJ, 914, 17
Levesque, E. M., & Richardson, M. L. A. 2014, ApJ, 780, 100
Li, J., Xue, Y., Sun, M., et al. 2019, ApJ, 877, 5
Liu, T., Tozzi, P., Wang, J.-X., et al. 2017, ApJS, 232, 8
Luo, B., Brandt, W. N., Xue, Y. Q., et al. 2017, ApJS, 228, 2
Luridiana, V., Morisset, C., & Shaw, R. A. 2015, A&A, 573, A42
Madau, P., & Dickinson, M. 2014, ARA&A, 52, 415
Maiolino, R., Salvati, M., Bassani, L., et al. 1998, A&A, 338, 781
Masters, D., McCarthy, P., Siana, B., et al. 2014, ApJ, 785, 153
Matharu, J., Papovich, C., Simons, R. C., et al. 2022, ApJ, 937, 16
Mendez, A. J., Coil, A. L., Aird, J., et al. 2013, ApJ, 770, 40
Mignoli, M., Vignali, C., Gilli, R., et al. 2013, A&A, 556, A29
Momcheva, I. G., Brammer, G. B., van Dokkum, P. G., et al. 2016, ApJS, 225, 27
Nakajima, K., & Ouchi, M. 2014, MNRAS, 442, 900
Olivier, G. M., Berg, D. A., Chisholm, J., et al. 2022, ApJ, 938, 16
Papovich, C., Simons, R. C., Estrada-Carpenter, V., et al. 2022, ApJ, 937, 22
Pérez-González, P. G., Cava, A., Barro, G., et al. 2013, ApJ, 762, 46
Pirzkal, N., Malhotra, S., Ryan, R. E., et al. 2017, ApJ, 846, 84
Pirzkal, N., Ryan, R., & Brammer, G. 2016, Trace and Wavelength Calibrations of the WFC3 G102 and G141 IR Grisms, Instrument Science Report WFC3 2016-15 STScI
Planck Collaboration, Aghanim, N., Akrami, Y., et al. 2020, A&A, 641, A6
Reback, J., Jbrockmendel, McKinney, W. 2022, pandas-dev/pandas: Pandas 1.4.2. Zenodo, doi:10.5281/zenodo.3509134
Rhoads, J. E., Wold, I. G. B., Harish, S., et al. 2023, ApJL, 942, L14
Simons, R. C., Papovich, C., Momcheva, I. G., et al. 2023, ApJ, arXiv:2303.09570, in press
Simons, R. C., Papovich, C., Momcheva, I., et al. 2021, ApJ, 923, 203
Skelton, R. E., Whitaker, K. E., Momcheva, I. G., et al. 2014, ApJS, 214, 24
Steidel, C. C., Rudie, G. C., Strom, A. L., et al. 2014, ApJ, 795, 165
Stern, D., Eisenhardt, P., Gorjian, V., et al. 2005, ApJ, 631, 163
Tang, M., Stark, D. P., Chevallard, J., et al. 2021, MNRAS, 501, 3238
Thuan, T. X., & Izotov, Y. I. 2005, ApJS, 161, 240
Trump, J. R., Arrabal Haro, P., Simons, R. C., et al. 2023, ApJ, 945, 35
Trump, J. R., Impey, C. D., Kelly, B. C., et al. 2011, ApJ, 733, 60
Trump, J. R., Sun, M., Zeimann, G. R., et al. 2015, ApJ, 811, 26
Veilleux, S., & Osterbrock, D. E. 1987, ApJS, 63, 295
Walter, R., & Fink, H. H. 1993, A&A, 274, 105
Waskom, M. 2021, JOSS, 6, 3021
Wuyts, S., Förster Schreiber, N. M., Lutz, D., et al. 2011, ApJ, 738, 106
Xue, Y. Q., Luo, B., Brandt, W. N., et al. 2011, ApJS, 195, 10
Xue, Y. Q., Luo, B., Brandt, W. N., et al. 2016, ApJS, 224, 15
Yan, R., Ho, L. C., Newman, J. A., et al. 2011, ApJ, 728, 38
Yang, G., Boquien, M., Buat, V., et al. 2020, MNRAS, 491, 740
Yang, G., Brandt, W. N., Luo, B., et al. 2016, ApJ, 831, 145
Zeimann, G. R., Ciardullo, R., Gebhardt, H., et al. 2014, ApJ, 790, 113
Zeimann, G. R., Ciardullo, R., Gebhardt, H., et al. 2015, ApJ, 798, 29